Gold and Zinc Oxide Nanoparticle Coated Peptide Nanotubes Fabrication and Their Electrical Transport Properties Study

By

Luona Anjia

A dissertation submitted to the Graduate Faculty in Chemistry in partial fulfillment of the requirements for the degree of Doctor of Philosophy, The City University of New York

2012

This manuscript has been read and accepted for the Graduate Faculty in Chemistry in satisfaction of the dissertation requirement for the degree of Doctor of Philosophy.

Prof. Hiroshi Matsui, Hunter College

Date

Chair of Examining Committee

Prof. Maria Tamargo

Date

Executive Officer

Prof. Charles M. Drain, Hunter College

Prof. Yujia Xu, Hunter College

Prof. Raymond Tu, City College

Supervisory Committee

THE CITY UNIVERSITY OF NEW YORK

Abstract

Gold and Zinc Oxide Nanoparticle Coated Peptide Nanotubes Fabrication and Their Electrical Transport Properties Study

by

Luona Anjia

Adviser: Prof. Hiroshi Matsui

There is a growing interest in attempts in using biomolecular as the 1D nanotube templates to grow inorganic nanoparticles (NPs) in controlled morphology and structure. One of the research motivations for this combination is to take advantage of the catalytic activity for the room-temperature material growth and the ability of self-assembly into controlled structures on a large scale. One approach to fabricate such nanotube is by using a glycine-based peptide nanotube as template, and on template sidewall immobilizing biomineralizing peptide, which can selectively bind to the target metal/semiconductor precursor and mediate the formation of the inorganic material on templates incorporating these peptides.

By optimizing the experiment conditions, we successfully fabricated high yield of nanotubes with full coverage of high-density monodispersed Au and ZnO NPs coating. Using drop casting technique, we built electronic device with these nanotubes and found

very interesting electrical transport properties: the temperature-dependent current-voltage characteristic of Au NPs nanotube; and the negative differential resistance property (current decreases with increasing bias voltage) of ZnO NPs coated nanotube. These results are of great impact on the future development of bio-nanoelectronic devices.

Besides, a new biomimetic approach for one-pod synthesis of ZnO nanotube at neutral pH and room temperature is introduced; by self-assembling peptides which possess the catalytic mineralization function for the specific oxide metal, ZnO nanotube can be grown as the peptides are simultaneously assembled into a rod structure and template ZnO growth in gels formed by the peptides and Zn precursors. Traditionally, biomineralizing peptides are coated on 1D templates and then grow ZnO at room temperature, however this new method allows one to grow ZnO nanotubes in one step without using 1D templates since the Zn-mineralizing peptide itself can be assembled into the 1D structure.

This is

dedicated to

My husband: Yangyang Xiao

谨以此文献予

在毕业冲刺阶段特地从中国新疆赶来美国纽约

支持陪伴我的母亲：何叶•晓荣女士

Acknowledgements

First and above all, I'd like to give my wholehearted gratitude to my dear mentor, Prof. Hiroshi Matsui, for his inspiring guidance, unconditional devotion, and enlightening instructions in the joyful but challenging journey of my PhD study.

I also own thanks to my research committee members, Prof. Michael C. Drain, Prof. Yujia Xu, Prof. Raymond Tu and Prof. Ronald L. Koder. This dissertation cannot be so fruitful without their continuous guidance and advice.

As a research collaborator, I own special thanks to Prof. Saiful I. Khondaker, Dr. Shashank Shekhar, Dr. Daeha Joung, Mr. Zengyan Wei, Ms. Menglu Shi and Mr. Wei Su. Our collaborating has been enjoyable and fruitful.

As strong technic support, I own special thanks to Dr. Jorge Morales, Dr. Areti Tsiola, Prof. Glen Kowach, Prof. Vinod. M. Menon, Prof. Igor L. Kuscovsky, Dr. Lijia Yang, Dr. Ruben Diaz-Avalos and Dr. William Rice.

I own thanks to my previous colleagues in our lab: Dr. Hanying Bai, Dr. Anita Swami, Dr. Xueyun Gao, Dr. Nurxat Nuraje, Dr. Roberto de la Rica, Dr. Linglu Yang, Dr. Lingtao Yu, Dr. Fen Xu, Dr. Jungsun Lim, Dr. Christophe Pejoux and current colleagues: Dr. Yoshiyaki Maeda, Dr. Yasuhiro Ikezoe, Ms. Prerna kaur, Ms. Kristina Fabijanic, Ms.Parminder Jeet Kaur, Mr.Wei Su, Ms. Ying Xu, Ms. Menglu Shi, and Mr. Zengyan Wei.

Most of all, I want to express my gratitude to my dear parents: mother Ms. Xiaorong Heye, father Mr. Zhicheng Anjia and my lovely husband Mr. Yangyang Xiao.

Table of Contents

List of Figures

List of Tables

Chapter 1. Introduction to the Peptide Nanotube Fabrication

Inorganic nanoparticles (NPs) have been heralded as potential building blocks for new materials with superior properties and applications.[1,2] To apply NPs as building blocks for practical electronic, magnetic, and optical devices, NPs must be assembled. Although various NPs have been assembled on flat substrates,[3-5] the self-assembly of NPs on cylindrical nanotube surfaces also emerged as another type of important building blocks in sensors and microelectronics.[6-9] There is a growing interest in attempts in using biomolecular as the 1D nanotube templates to grow such inorganic NPs in controlled morphology and structure. One of the research motivations for this combination is to take advantage of the catalytic activity for the room-temperature material growth and the ability of self-assembly into controlled structures on a large scale.[8, 10, 11-13]

To achieve above results, biomineralizing peptides need to be coated on the 1D templates first, and then grow inorganic NPs on surface of biomineralizing peptide coated template nanotube at room-temperature. Most of these biomineralizing peptides were engineered using combinatorial library approaches such as phage display and cell-surface display,[14-19] and these peptides exhibiting high binding affinities for specific inorganic materials are capable to mediate the formation of specific inorganic material on templates incorporating these peptides.

Previously, various biomineralizing peptide were incorporated on peptide nanotube surfaces.[8, 20-24] These templating bionanotubes were self-assembled from glycine-based peptide monomers, bis(*N*-α-amido-glycylglycine)-1,7-heptane dicarboxylate, via three-

dimensional hydrogen bonds between amide and carboxylic acid groups (Figure1.1), and these templating bionanotubes could bind various synthetic peptide at the free amide groups on the nanotubes surfaces with hydrogen bonding with the simple incubation process.[25] When this template nanotube immobilized the mineralizing peptides on the nanotube surface, these immobilized peptides could nucleate metal/semiconductor NPs on the templating bionanotubes (Figure 1.2, 1.3).

Figure 1.1 (a) Transmission electron micrograph (TEM) of the template nanotube. (b) Chemical structure of peptide bolaamphiphile monomer. (c) Chemical structure of the template nanotube from the monomer (b). The template nanotube surface has free amide groups (shown by arrows and yellow squares) to immobilize biological molecules on the nanotube surfaces.[8]

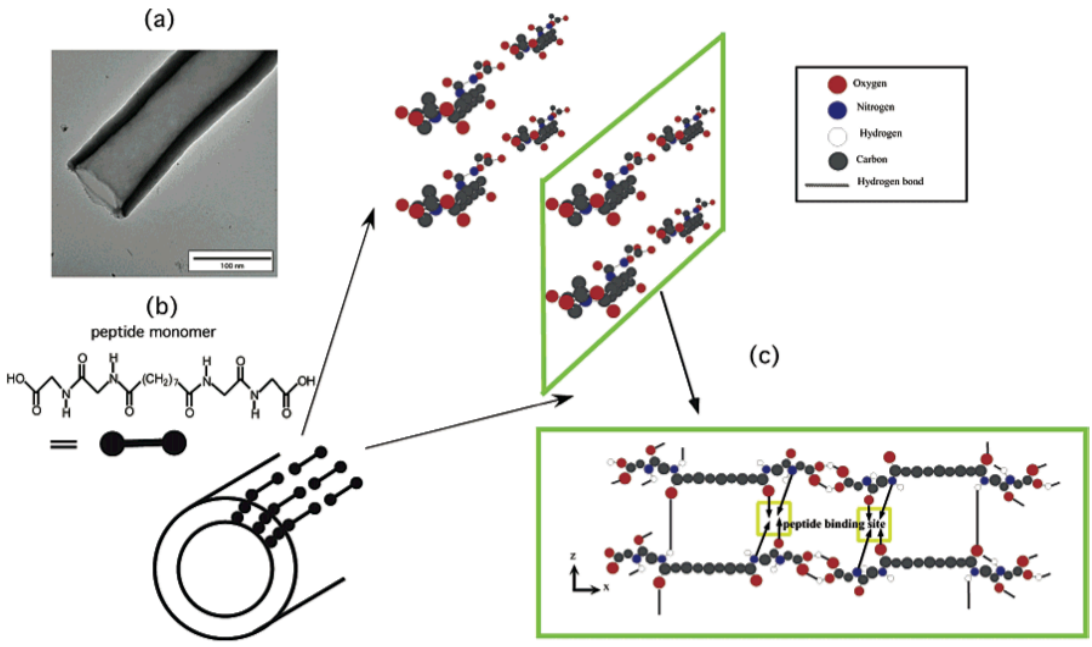

Figure 1.2 TEM images of Au nanocrystals on the sequenced histidine-rich peptide nanotubes grown by reducing the Au ion-nanotube solution after incubating Au ions for 10 days at (a) pH 8 and (b) pH 11.5. Insets show the TEM images in higher magnification.[8]

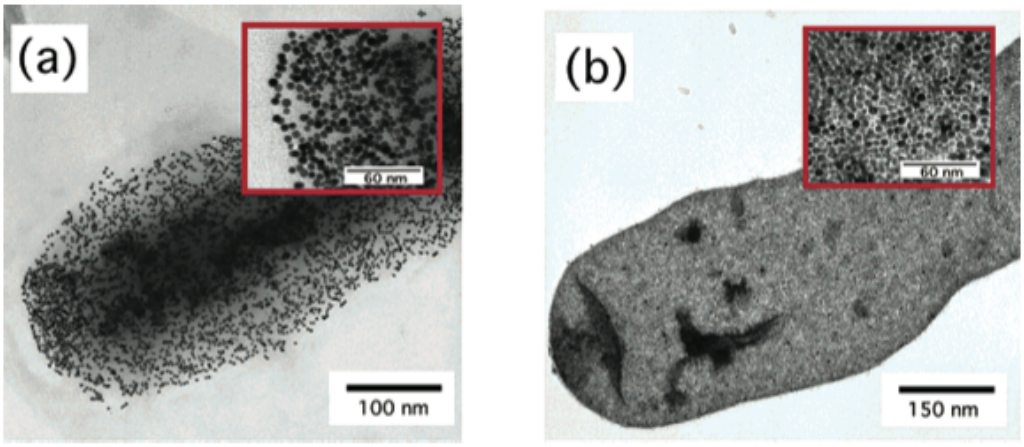

Figure 1.3 TEM images of Cu_2S nanocrystals grown on the H12 peptide-coated nanotubes at (a) pH 5 (b) pH 8. Scale bar = 70 nm. Insets show the electron diffraction patterns that correspond the hexagonal structure.[26]

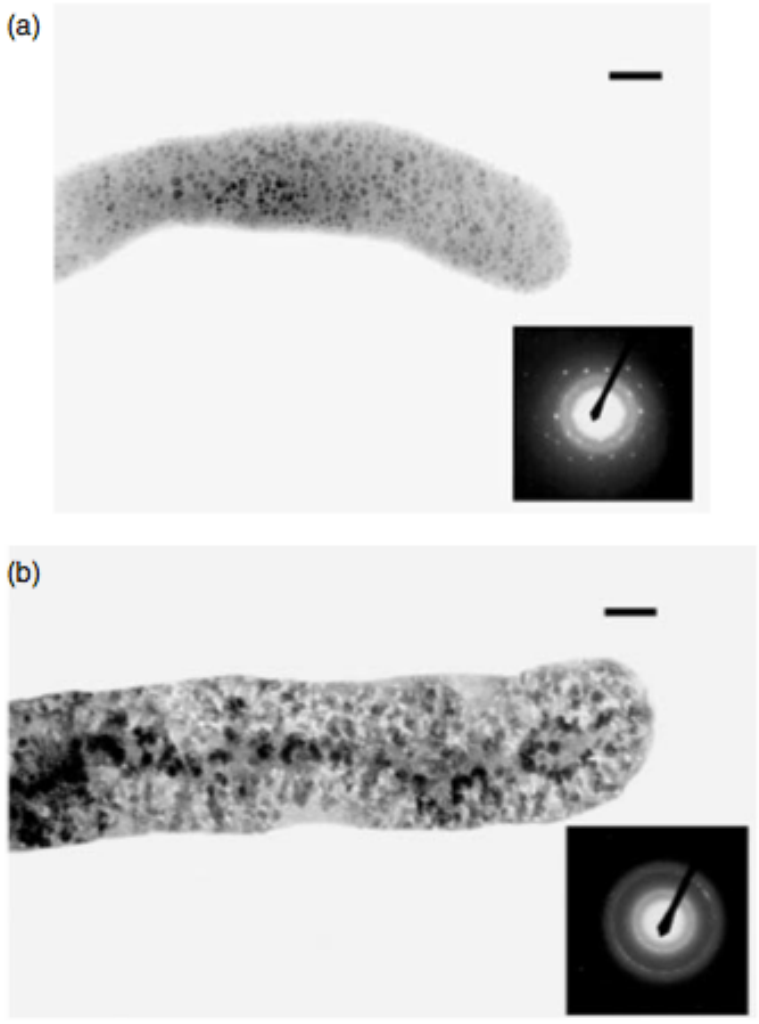

Figure 1.4 Scheme of the Au nanowire fabrication. (a) Immobilization of the sequenced histidine-rich peptide at the amide binding sites of the template nanotubes. (b) Au ion immobilization on the sequenced histidine-rich peptide. (c) Au nanocrystal growth on the nanotubes nucleated at Au ion-binding sites after reducing Au ions with hydrazine hydrate.[8]

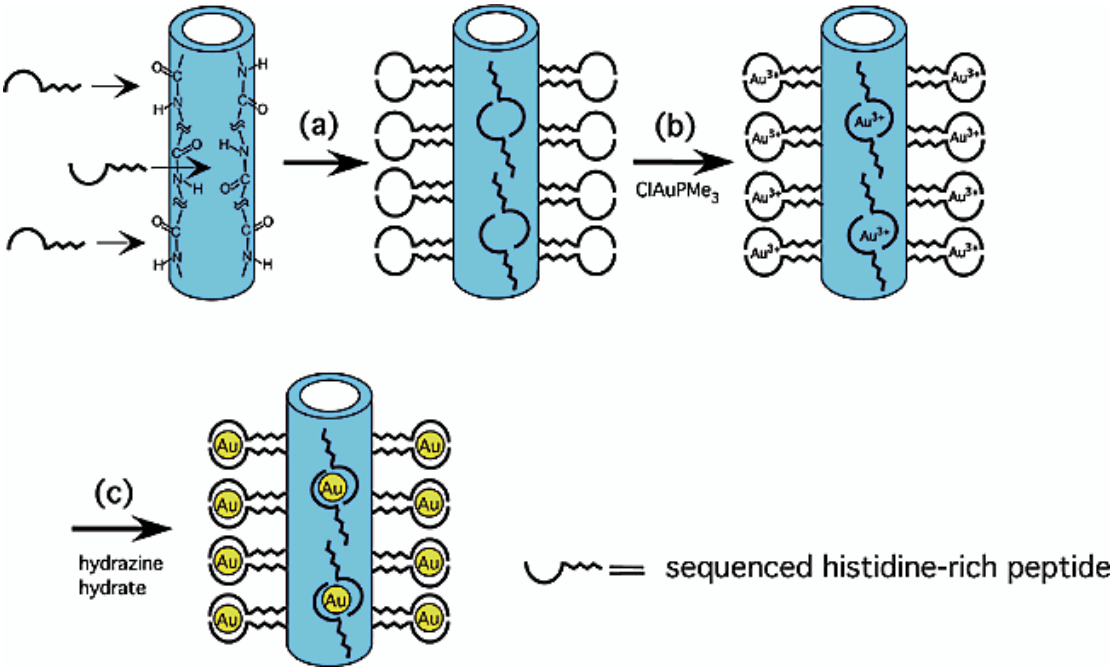

The general procedures to fabricate such metal/semiconductor nanoparticles coated peptide nanotube are: **a)** Find the proper mineralizing peptide from published literatures, immobilize the peptides onto the surface of nanotube template at free amide sites of the sidewall via hydrogen bonding (Figure 1.1c); **b)** Add the precursor, ion or complex form of the key element in the target coating material ($ClAuPMe_3$ for Au coating,[8] Cu^{2+} for Cu_2S coating,[26] Zn^{2+} for ZnO coating,[9] etc.), into the solution of peptide nanotube coated with mineralizing peptide. The biological recognition of the mineralizing peptide selectively trap the target element ions for the nucleation; **c)** Add the reducing agent for metal NPs growth, or Na_2S for semiconductor NPs containing sulfur such as Cu_2S, or NaOH for oxide material such as ZnO. An example of Au nanotube fabrication procedure is illustrated in Figure 1.4.

Most of these previous published results were focused on the nanotube fabrication and exploring the mechanism of changing the coated NPs morphology and coating density.[8, 9, 21-24, 26, 27] To actually use these nanotubes as building blocks in electronics, we have to consider another important issue to further optimize the fabrication results – the yield. Due to the small size of these nanotubes, it is difficult to pinpoint the individual best coating nanotube and put it into our device. Instead, drop casting is the technique used very often for building a micro-device nowadays. A drop of nanotube solution contains lots of nanotubes, if only a small portion of the tubes were well coated with the target material, it would be very hard to actually build a working device, since the nanotubes with poor coating are much more likely to be aligned into the device. Thus, in the following chapters involving electrical property studies (see detail in Chapter 2 and 3),

behind each final fabrication procedure a lot of effort was put into optimizing the NPs coating density and nanotubes coating yield.

To get a satisfying NPs coating density on the nanotube surface, many experiment parameters have been discussed previously,[8, 9, 21-24, 26, 27] like the relative concentration of mineralizing peptides and precursors, the incubation pH for peptide configuration change and NPs growth, the incubation time length, the buffer species used in the incubation process to maintain certain pH value, and so on. However, there is another important parameter that has not been discussed previously – the hydrophilicity of the mineralizing peptide. Although the peptide can bind to the template bionanotubes via hydrogen bonding as discussed before, the hydrophilicity of peptide was found to influence the coating result as well. Since the mineralizing peptide is the necessary linker between the NPs grown from precursor and the template bionanotubes, the peptide affinity to the bionanotubes, or to say the peptide coating efficiency, influence the NPs coating density significantly.

Figure 1.5 TEM images of Au NPs coated bionanotubes incubated at pH 7.0 with 1 day Au precursor incubation, (a) Using HRE peptide as the mineralizing peptide (scale bar = 500 nm), (b) close up view of (a), scale bar = 20 nm. (c) Using NHBP-1 peptide as the mineralizing peptide (scale bar = 200 nm), (d) close up view of (c), scale bar = 10 nm.

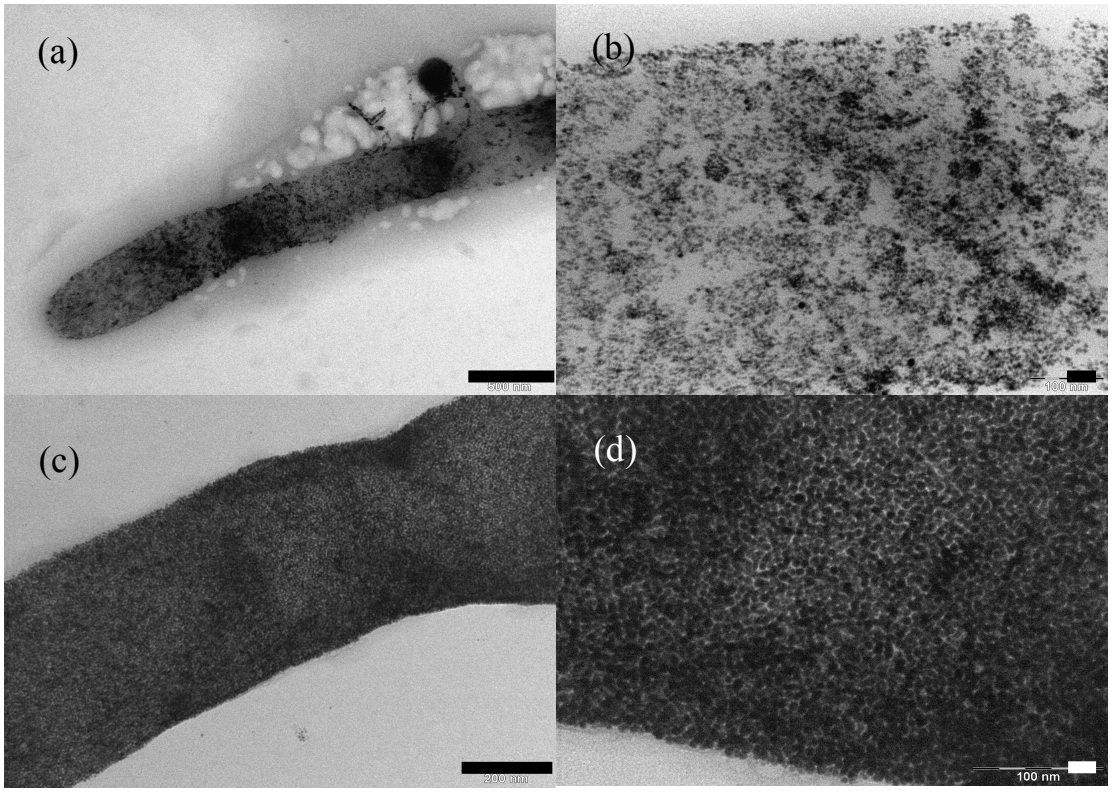

NHBP-1 peptide (DYFSSPYYEQLF) and HRE peptide (AHHAHHAAD) are both Au-mineralizing peptide.[8, 28] When these two peptides were used in the Au nanotube fabrication with exact same experiment conditions, the Au NPs coating density in NHBP-1 peptide case is much higher than the HRE peptide case (Figure 1.5). The main difference of these two peptides is the hydrophilicity. NHBP-1 peptide is over all more hydrophobic than HRE peptide (Figure 1.6).

Figure 1.6 Hydrophilicity plots[29] of (a) NHBP-1 peptide, (b) HRE peptide.

(a)

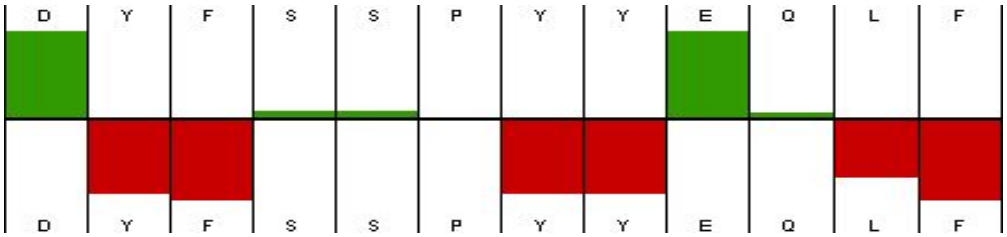

Average hydrophilicity: -0.6

(b)

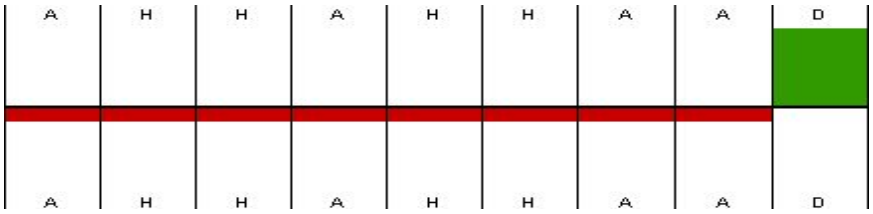

Average hydrophilicity: -0.1

In Figure 1.6, the hydrophilicity for each amino acid in a peptide sequence are plotted in a bar graph using Hopp –Woods hydrophilicity scale[29]: more hydrophobic amino acid is plotted with longer red bar (more negative hydrophilicity); more hydrophilic amino acid is plotted with longer green bar (more positive hydrophilicity). And the average hydrophilicity is calculated with the same scale: more negative average hydrophilicity value represents a more overall hydropobic peptide; more positive average hydrophilicity value represents a more overall hydrophilic peptide.

From the comparison of NHBP-1 and HRE peptides Au NPs coating results (Figure 1.5), it seems hydrophobic peptide has higher affinity to the template bionanotube used in this system. This property is not hard to explain if we look at the molecular structure of the template bionanotube (Figure 1.1): there is a seven-carbon chain in each monomer, and such hydrophobic carbon chains are spread out the entire surface of the self-assembly bionanotube. These wide spread hydrophobic regions on nanotube surface can bind with hydrophobic peptide via hydrophobic-hydrophobic interaction. Thus, besides the hydrogen bonding, hydrophobic peptides have one more binding force, compared with less hydrophobic peptide, to enhance the affinity to the template bionanotube.

Figure 1.7 Hydrophilicity plots[29] of (a) J140 peptide, (b) ZnO-1 peptide. TEM images of (c) CdSe NPs coating using J140 peptide, (d) ZnO NPs coating using ZnO-1 peptide. (Scale bar = 100 nm).

(a)

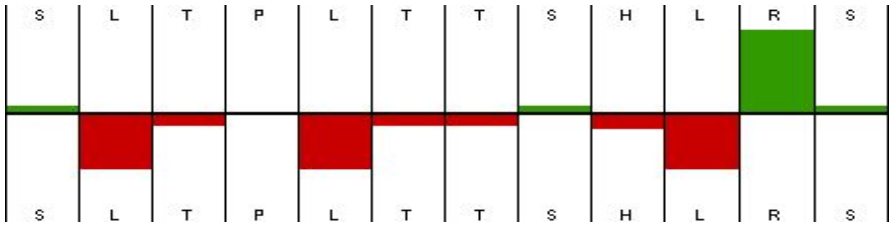

Average hydrophilicity: -0.3

(b)

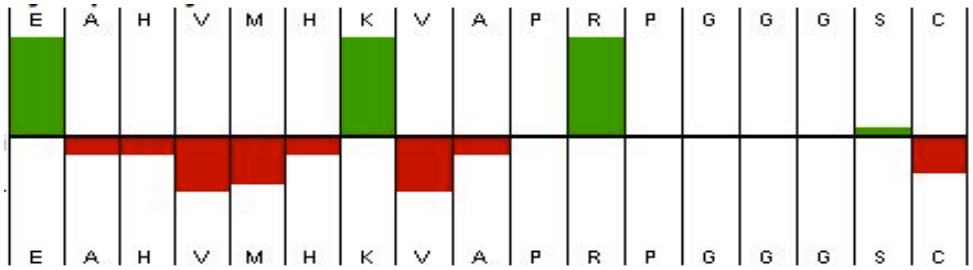

Average hydrophilicity: 0.1

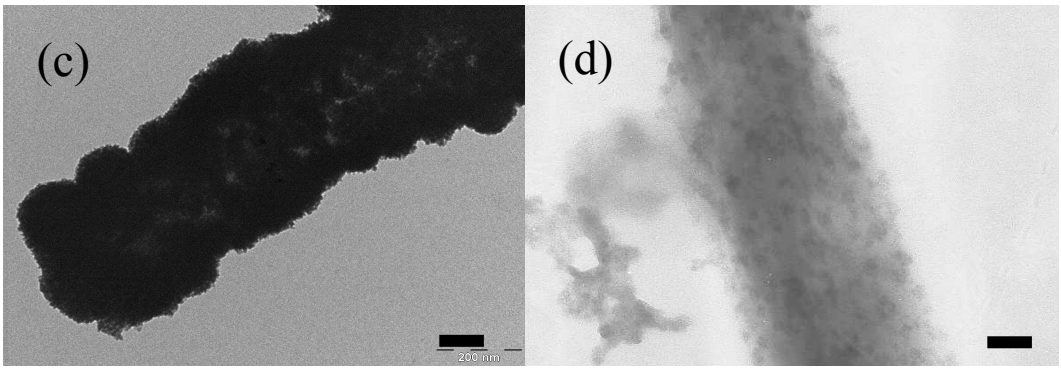

This hypothesis was also supported by other material coating results. CdSe NPs were easily coated on bionanotube with extreme high coating density when a hydrophobic mineralizing peptide J140 (SLTPLTTSHLRS)[30] was used (Figure 1.7a,c). ZnO NPs were coated only on very few bionanotubes with low coating density even after many times of optimization when using a hydrophilic peptide ZnO-1 (EAHVMHKVAPRPGGGSC)[15] (Figure 1.7b,d).

However, it does not mean that the more hydrophobic the mineralizaing peptide is, the better the NPs coating result is. One reason is that an over hydrophobic peptide is very hard to be dissolved in water solution. Second, when the peptide is hydrophobic enough and able to form its own self-assembly structures, these peptide will not bind to the template bionanotube. In this second case, it is possible to fabrication NPs coated nanotubes without using the 1D template (see detail in Chapter 4).

Although there are many different biomineralizaing peptide synthesized, the available peptides for certain metal/semiconductor material is not that much that we cannot freely pick a peptide with the desired hydrophilicity. In this case, an expedient method can be used by covalently binding the peptide with the template bionanotube (see detail in Chapter 3).

Chapter 2. Electrical Transport Properties of Peptide Nanotubes Coated with Gold Nanoparticles via Peptide-induced Biomineralization

Introduction

Nanocrystals of sub-10 nm dimensions are of intense research interest because of their size-dependent electronic and optical properties and their potential applications as a building block for future generation of nanoelectronic and photonic devices.[31-33] The conventional synthesis methods include ball milling, chemical vapor deposition, and solvothermal methods, however in general extreme physical and chemical growth conditions are necessary to control their syntheses, morphologies, and assemblies.[34,35] To assemble these materials into specific geometries for their potential applications, techniques such as Langmuir-Blodgett, self-assembly, crosslinking precipitation, DNA-based scaffolds, and fluidic flow-directed assembly have been applied.[35-38] Recently, one approach that has attracted considerable attention, is the biological route of material synthesis due to its ability to synthesize nanomaterials in precise sizes and shapes in environmentally benign conditions as well as its ability to self-organize and assemble these materials in various geometries using biomolecules such as virus, protein, DNA, and peptide.[8, 20, 39, 40] The progress have been made for the biological route of material synthesis and assembly for nanodevice development, however, detailed electronic transport investigation of these materials is not explored in depth for the application of nanoelectronics.

In this chapter, we report temperature-dependent (300-4.2 K) electrical transport behavior of peptide nanotubes coated with monodisperse gold nanoparticles (AuNPs) in the diameter of 6 nm. The current-voltage (*I-V*) characteristic of this inorganic-biomolecular hybrid nanotube is linear at room temperature in the voltage region -1 V to 1 V and the resistance (*R*) is ~3 MΩ corresponding to a lattice conductivity of ~ 0.44 S/cm. As the temperature is lowered, the *I-V* curves become increasingly non-linear and below 20 K a finite threshold voltage V_T is needed for charge conduction with the current following the scaling behavior $I \propto [(V - V_T)/V_T]^{\alpha}$ with $\alpha \sim 2.5$ for $V > V_T$. The temperature dependence of the resistance shows thermally activated hopping behavior with an activation energy of 18.2 meV, in good agreement with sequential tunneling of charges through 6 nm sized 2D quantum dots arrays. Our results here regarding the conduction mechanism of large-scale AuNP arrays on the peptide templates are of great importance to the future development of bio-nanoelectronic devices.

Figure 2.1 (a) Transmission electron micrograph of a typical AuNPs coated peptide nanotube showing the particles are monodisperse with an average size of 6 nm. (b) Scanning electron micrograph of a typical device with 1 μm electrode separation.

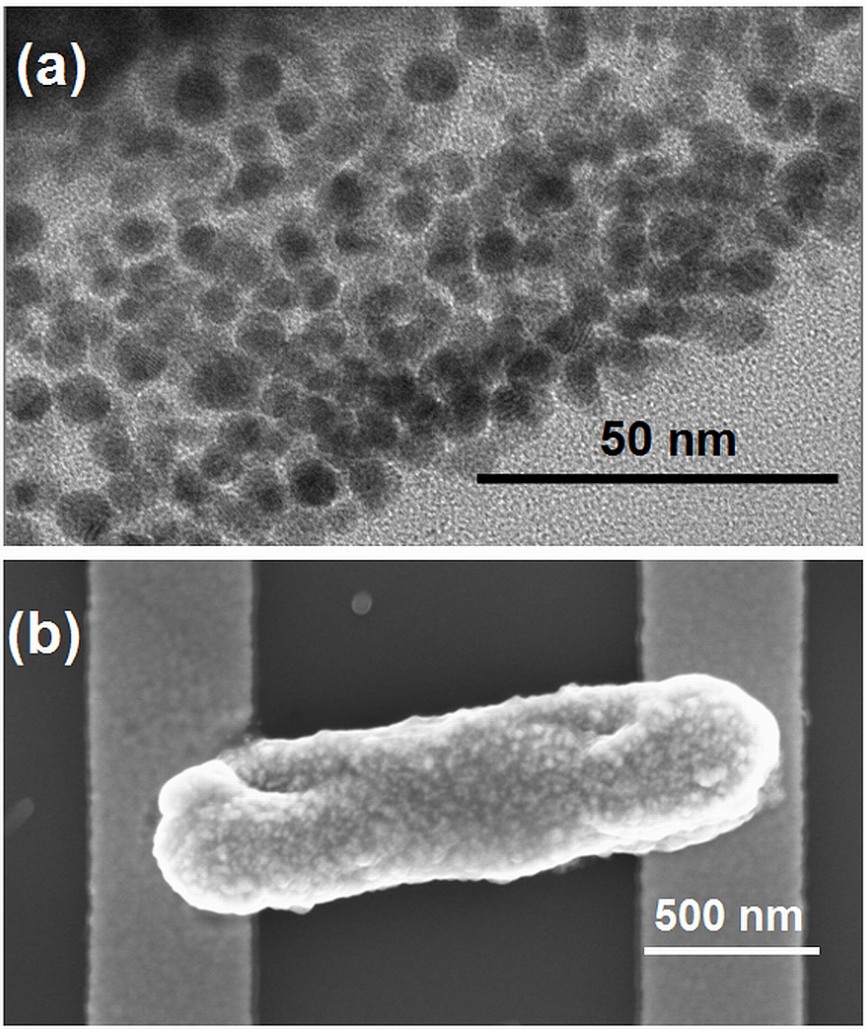

Experiments

The template peptide nanotube (PNT) was self-assembled from bis(N − α-amido-glycylglycine)-1,7-heptane dicarboxylate monomers (3 mM) in a pH 4.5 citric acid/NaOH solution. Details of this bolaamphiphile peptide monomer synthesis and the nanotube self-assembly have been described elsewhere.[8] The NHBP-1 peptide, DYFSSPYYEQLF (purity > 90%), was obtained from GenScript and reported to mineralize Au with the aid of a reducing agent.[41] To immobilize the NHBP-1 peptide on the template nanotubes, 1 ml of the peptide solution (2 mM) in Tris buffer (0.1M, pH 7) was incubated 24 h with 50 μl of the template nanotube solution that has been washed with deionized water several times by centrifuging (14,000 rpm, 45 min). The coated nanotubes were washed with deionized water several times by centrifuging to remove any unbound NHBP-1 peptide. Citric acid (0.1M) and NaOH (0.1M) were added to the peptide nanotube solution to adjust pH to pH 10. To grow Au nanocrystals on the NHBP-1 peptide nanotubes, 4mg of $ClAuPMe_3$ was mixed with the peptide nanotube solution (1 ml) in the dark at room temperature. After the mixture was allowed to sit for five days to complete immobilization of Au ions on the peptide nanotubes and any extra $ClAuPMe_3$ was removed, 50 μmol of a reducing agent, hydrazine hydrate, was added to produce Au coating on the nanotubes. After 24 h, the Au nanotubes were washed with deionized water several times by centrifuging to remove excess reducing agent. After above incubation, monodisperse AuNPs of diameter 6 nm were grown on the peptide nanotubes. Figure 2.1(a) shows a transmission electron micrograph (TEM) of AuNPs coated on one of the peptide nanotubes. From this image, we determined an average diameter of the AuNP to be 6 nm with an average interparticle separation of 1 nm. In addition, AuNPs

are homogeneously distributed over the cylindrical nanotube surface. Selected area electron diffraction (SAED) of the AuNP nanotube showed (111), (200), and (220) planes of Au (see Figure S2.1 in supplementary information). Control experiment was carried out to confirm the function of NHBP-1 peptide: Au nanocrystals were grown directly on the neat nanotubes at pH10 with no NHBP-1 peptides coating on the nanotubes. The experimental condition was the same as above except that no NHBP-1 peptide was coated on the nanotubes before incubating Au precursor. From the TEM image of control experiment result (see Figure S2.2 in supplementary information), much less Au NPs were coated and the coating was not uniform, and the NPs were polydisperse in diameter.

For electrical measurements, electrodes were fabricated on standard heavily doped silicon substrates capped with a thermally grown 250 nm thick SiO_2 layer, by a combination of optical and electron beam lithography. The electrodes consisted of an interdigitated array of 1 μm spacing. After defining the patterns, 3 nm Cr and 30 nm thick Au were deposited followed by lift off in acetone. The electrodes were then treated in oxygen plasma for 10 min to remove any residual organics. The AuNP coated peptide nanotubes were placed between the electrodes by the drop casting method. Figure 2.1(b) shows a scanning electron microscopy image of a fabricated device with a PNT of diameter ~0.4 μm and length ~1.5 μm placed between source and drain electrodes. The samples were then bonded and loaded into a variable temperature cryostat. The electrical measurements were performed using a current preamplifier (DL instruments 1211) combined with a high resolution DAC card interfaced with LabView, capable of measuring pico-ampere current.

Figure 2.2 (a) *I-V* characteristic for a AuNP-coated peptide nanotube for temperatures 30, 20, 15, 10 and 4.2 K. Below 20 K, a finite threshold voltage V_T is needed for the charge conduction. Inset is I-V curve at 300 K. (b) *I* versus $(V-V_T)/V_T$ curves plotted in a log-log scale. The slope of the curves provides the exponent α= 2.4–2.6; inset shows the dependence of V_T on T.

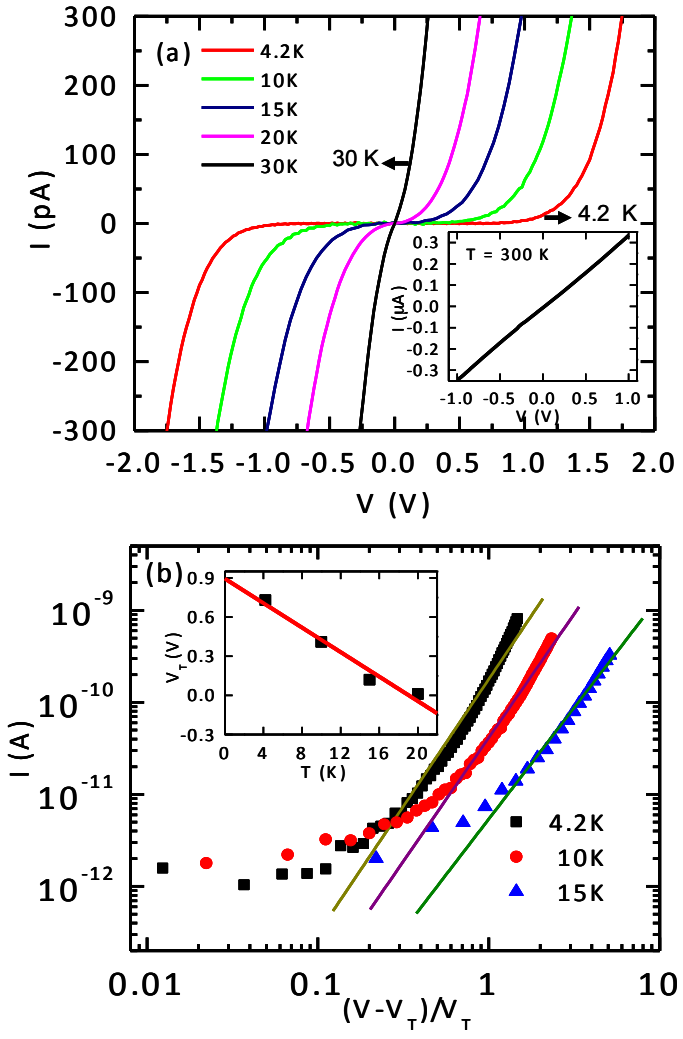

Results and Discussions

The inset in Figure 2.2(a) shows the *I–V* characteristics of a representative device at room temperature (300 K) containing one PNT. The *I–V* curve is linear in the range of −1–1 V and shows a resistance value of ~3 MΩ. This corresponds to a lattice conductivity of ~0.44 S cm^{-1} assuming the charge conducts through the outer layer of the PNT where AuNPs are conjugated with a cross-sectional area of ~4π R_P r , with R_P and r are the radius of the PNT and the AuNP respectively. The PNT does not contribute to conduction as the controlled experiment showed no noticeable current. As the temperature is lowered, the *I–V* curves become increasingly nonlinear near zero-bias but remain symmetric at all temperatures. This is shown in Figure 2.2(a) where we present the data for T = 30–4.2 K. It can be seen from here that, below 20 K the charge conduction is completely blocked below a certain threshold voltage V_T. This is due to the Coulomb blockade of charges as there is not enough thermal energy for charges to overcome the Coulomb charging energy of the AuNP quantum dot (QD) arrays on the nanotube. The lower the temperature is, the larger the V_T. The measured values of V_T were 10 mV at 20 K, 120 mV at 15 K, 410 mV at 10 K, and 730 mV at 4.2 K.

The voltage dependence of current above V_T depends on the number of accessible current paths through the AuNP assembly (superlattice). It is predicted that for a uniform array of identical nanoscale metallic islands separated by tunnel barriers, the current should follow $I \propto [(V - V_T)/V_T]^{\alpha}$ for $V > V_T$, where α is the scaling exponent that depends on the dimensionality of the array.[42] Figure 2.2(b) shows current plotted versus $(V - V_T)/V_T$ in a log–log scale for T = 15, 10, and 4.2 K. The symbols are the experimental data points while the solid lines are a fit to the above equation. The data are fitted for

voltages away from V_T, as close to V_T the current is within the experimental error limit. From these fits, we obtain α to vary between 2.4 and 2.6. In the one-dimensional case there is one current carrying path and α should be unity.[42] For a two-dimensional (2D) array of nanoparticles, the theoretical value of α was predicted as 1.6 while numerical simulations yielded 2.0,[42] but an experimentally higher value of α (~ 2.5) was observed .[43, 44] Our α value implies that the AuNP arrays on the cylindrical surface of the PNT provide 2D charge conduction pathways.

The inset in Figure 2.2(b) shows the V_T versus T plot. V_T increases linearly as temperature decreases and extrapolation of this plot to 0 K provides the global threshold voltage V_T^0 = 890 mV. At 0 K, charge conduction through AuNPs takes place only when a potential higher than the total barrier of the AuNP QD array is applied between the electrodes and V_T^0 can be expressed as $V_T^0 = \beta N E_C/e$ [14] where, E_c is the charging energy of AuNPs, N is the number of AuNPs in the conduction path, and β is a proportionality constant whose value depends on the dimensionality of the system and for a 2D array β = 0.3.[42, 45] In our devices where electrodes are separated by ~1 μm (see figure 2.1(b)), nearly 140 AuNPs are required to bridge the gap since each AuNP of diameter 6 nm and interparticle separation of 1 nm occupies 7 nm of space. Using these values, we obtain E_c = 21.2 meV. E_c can also be calculated from the geometry and capacitance of the assembly and is given by $E_c = e^2/2C_\Sigma$, where C_Σ is the total capacitance and can be expressed as $C_\Sigma = 6C + C_g$. Here C and C_g are interparticle capacitance and self-capacitance of the quantum dot, respectively.[44] The factor of six appears due to the number of nearest neighbors for the 2D system.[44] The values of C and C_g are given by C

~ $2\pi\varepsilon_0\varepsilon r \ln(1 + r/d)$ and $4\pi\varepsilon_0\varepsilon r$, respectively, where r is the nanoparticle radius (3 nm), $2d$ is the interparticle distance (1 nm), and $\varepsilon(1)$ is the dielectric constant of the tunnel barriers (vacuum). By using these relations and values, the C_Σ is calculated to be 4.26 aF and E_c to be 18.8 meV, which is in excellent agreement with the value measured from the global threshold voltage. The estimated value of E_c via the charge tunneling through peptide (ε = 5) [46] is 6.7 meV. Since this value is much lower compared to the measured one, we conclude that the peptide acts as a template of AuNP growth but it does not contribute to the charge conduction.

Figure 2.3 (a) Resistance *R* plotted versus temperature in a semi-log scale showing four orders of change in *R* in the temperature range 4.2-260 K. (b) Reduced activation energy *W* versus *T* on a log-log scale. The slope $p = -1$ indicates the activated hopping mechanism. (c) Arrhenius plot of *R* versus T^{-1} (semi-log-scale) for the determination of activation energy E_c. We obtain $E_c = 18.2$ meV.

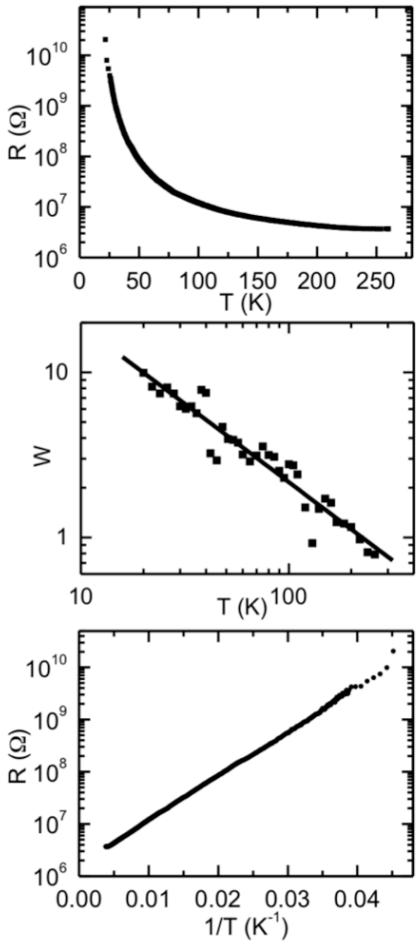

In order to further understand the electronic transport mechanism through the AuNP coated PNT, we study the temperature dependence of resistance of our devices. The temperature dependence of resistance can provide evidence about monodispersity of Au NPs and the degree of disorder of the NP assembly.[47, 48] Figure 2.3(a) shows the R versus T plot in the temperature range of 260–20 K. R was calculated by measuring current at a constant V = 20 mV as the temperature was lowered. We have also measured I– V curves at a few selected temperatures and obtained the R values from the ohmic part of the I–V curves. The R values were in agreement from the two measurements. Below 20 K, the I–V curves were non-ohmic below 20 mV and those data were discarded from this plot. It can be seen from Figure 2.3(a) that R changes by over four orders of magnitude in the temperature range of 260–20 K. According to the QD array model, if QDs are monodisperse, the temperature dependence of resistance should follow thermally activated behavior $R \sim R_0 \exp(E_c/K_BT)$,[47, 49] while if the nanocrystals have significant size variation (polydispersed) it should follow $R \sim R_0 \exp(T_{ES}/T)1/2$,[47, 50] where T_{ES} is a material constant related to the disorder of the material. In order to determine the exponent value we have considered a generalized formula $R(T) = R_0 \exp(T_0/T)^p$ and calculated the value of p from log W = $A - p$ log T, where $W = -\partial \ln R(T)/\partial \ln T = p(T_0/T)^p$ is the reduced activation energy and A is a constant.[51] By plotting log W versus log T, the value of p can be determined from the slope of this plot. Figure 2.3(b) shows W versus T plot in a log– log scale from which we calculate p = 1 signifying an activated hopping conduction mechanism. The agreement between the theory and the measurements also confirms that the size of AuNPs is monodisperse and their distribution is homogeneous. In order to derive the activation energy of the hopping conduction, R

can be fitted to T^{-1} on a semi-logarithmic scale, as shown in Figure 2.3(c). The fitting is linear over four orders of change in R over the entire temperature range. From the slope of this activation plot we calculate E_c = 18.2 meV, in excellent agreement with the E_c obtained from the capacitance calculation and global threshold voltage data. It should be noted that similar temperature dependences of the I –V curve, activated hopping, and charging energy were reproducible with three other AuNP array samples that we have studied.

Conclusions

In conclusion, we presented detailed electrical transport properties of peptide–AuNP hybrid bionanotube devices coated with gold nanoparticles (AuNPs) of 6 nm diameter within the temperature range of 300–4.2 K. We show that with the reduction of temperature, the I–V curves become increasingly nonlinear and below 20 K a finite threshold voltage V_T is needed for charge conduction. For $V > V_T$, the current follows $I \propto [(V - V_T)/V_T]^{\alpha}$ with $\alpha \sim 2.5$, suggesting that the charge conduction is through 2D arrays of AuNPs on the peptide assembly. The temperature dependence of the resistance shows thermally activated hopping behavior with an activation energy of 18.2 meV, in excellent agreement with the sequential tunneling model of charge transport through 6 nm size AuNP quantum dot arrays. Our results presented here regarding the conduction mechanism of large AuNP arrays on the peptide templates are of great importance to the future development of bio-nanoelectronic devices.

Supplementary Information

Figure S2.1 Selected area electron diffraction (SAED) of AuNP nanotube surface.

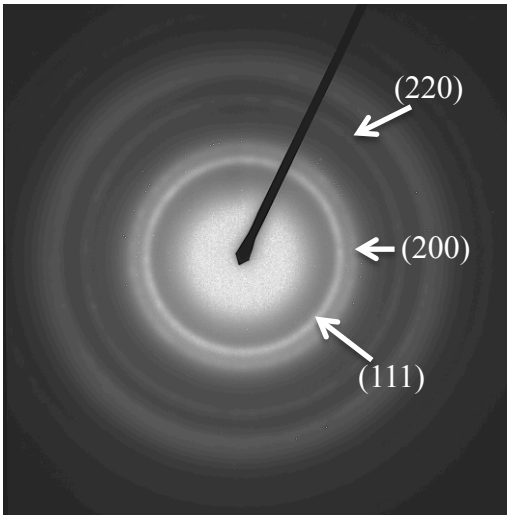

Figure S2.2 TEM image of the control experiment, Au coating nanotube without the NHBP-1 peptide. (Scale bar = 200 nm)

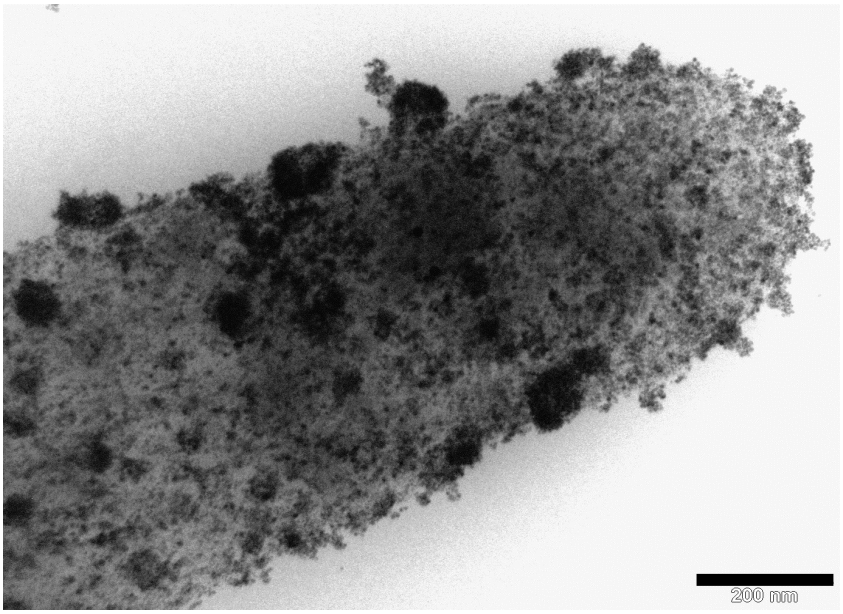

Chapter 3. Negative Differential Resistance in ZnO Coated Peptide Nanotube

Introduction

There is a growing interest in the realization of negative differential resistance (NDR), a nonlinear transport phenomenon where current suddenly decreases with increasing bias voltage, in different material systems as it constitutes an active component for building logic circuits, oscillator, diodes, memory, switches and sensors.[52-58] Recently, bio-template methods of material synthesis have been exploited for the creation of multifunctional materials for electronic and optoelectronic applications using biological scaffolds such as DNA, virus, protein, and peptide due to their high degree of organization, ease of chemical modification, and self assembly properties. [8-15] In addition, the capabilities to self-organize and control assembly in various geometries make them an attractive candidate for fabricating various functional devices in the form of one-, two-, or three- dimensional nanostructures. [20, 59, 60-65] Some of the reports indicate that the function of the templates is not only to provide a back bone for organization of discrete nanomaterials, but also to create novel electronic effects while integrated with nanomaterials.[65] These bio-templated nanostructures have shown useful applications in photocatalysis, battery, and memory devices. [62-65] However, the NDR phenomenon has not yet been observed in the bio-templated systems.

In this chapter, we report room temperature NDR behaviors on ZnO coated peptide nanotube contacted with Au electrodes by measuring current-voltage (I-V) characteristics. The NDR behaviors were found to be highly sensitive with the direction of voltage sweep,

scan rate, and humidity. We discuss the origin of NDR is due to the redox reaction of water molecules absorbed on the surface of ZnO coated peptide nanotube.

Figure 3.1 (a) TEM image of ZnO coated peptide nanotubes. Mean diameters of the nanotubes are ~ 400 nm and lengths are ~ 4 µm. (b) HRTEM image of the ZnO coated peptide nanotubes surface. (c) PL spectra of ZnO coated peptide nanotube at room temperature (λ_{ex}: 325 nm) (d) Schematic diagram of the device structure and measurement set up. Inset shows optical microscopic images of ZnO coated peptide nanotube on the Au electrodes.

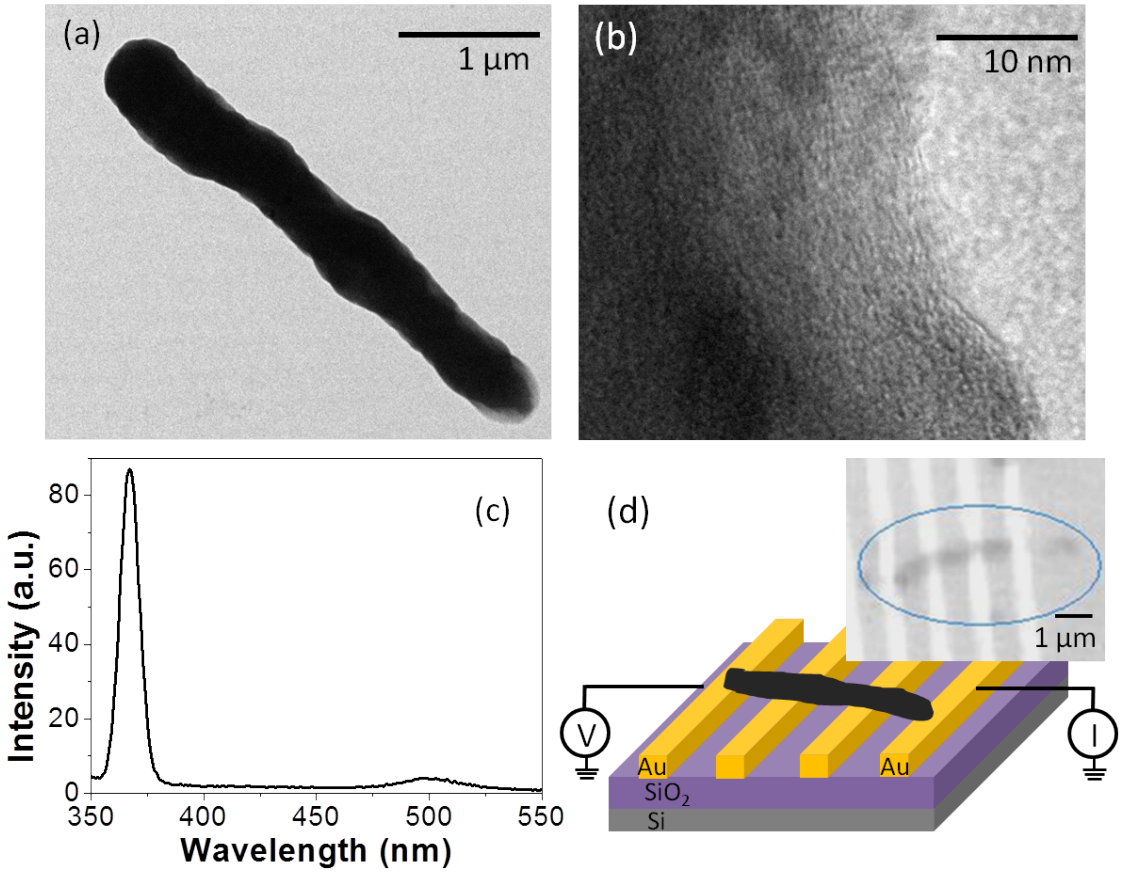

Experiments

The peptide nanotubes used for the ZnO mineralization were self-assembled from bis(*N*-α-amido-glycylglycine)-1,7-heptane dicarboxylate monomers. Details for the monomer synthesis and the method for the cylindrical self-assembly were described elsewhere.[16] In brief, the GGGSC-conjugated ZnO-1 peptide, whose sequence is EAHVMHKVAPRPGGGSC, was found to have high affinity to ZnO and can mediate the mineralization of ZnO from $Zn(OH)_2$ at room temperature.[15] To covalently bind amine groups of the ZnO-1 peptide with carbonyl groups of the nanotubes, the nanotubes were treated with NHS/EDAC reaction in MES buffer (0.1M, pH 5.5) first. After rinsing with deionized water to eliminate extra NHS, EDAC, and the remaining MES buffer, ZnO-1 peptide (2mM) was incubated with the CO-NHS ester group decorated nanotubes in HEPES buffer (0.1M, pH8). Zinc Acetate (0.5mM) was added after eliminating the extra peptide by rinsing with deionized water, then incubated for 3 days. Next, NaOH (1.5mM) was added and incubated for a day. Finally, unreacted NaOH was rinsed after incubation. Figure 3.1 (a) shows the transmission electron microscopy (TEM) images of a nanotube with a mean diameter and length of ~ 400 nm and ~ 4 μm, respectively. Figure 3.1 (b) shows the high resolution TEM (HRTEM) images of the nanotubes. The darker region is closer to the center of the nanotube axis and has more ZnO, while the lighter region is at the edge of the nanotube which has less ZnO. In order to further confirm the presence of ZnO, the photoluminescence (PL) spectra of ZnO coated peptide nanotube were performed on a Horiba Fluoromax 3 fluorescence spectrophotometer with an excited wavelength of 325 nm. This is shown in Figure 3.1(c) where we obsrved a strong characteristic near band edge emission of ZnO around 370 nm, and a weak blue emssion

near 500 nm that resulted from the presence of oxygen vacancies on surface of ZnO.[67] In addition, neither electron diffraction pattern, nor grain boundary was observed under TEM, indicating that the ZnO grown on peptide nanotube is amorphous.

ZnO coated peptide nanotube devices were fabricated on doped silicon (Si) substrates capped with a thermally grown 250 nm thick SiO_2 layer. Source and drain electrode patterns with interdigitated arrays of 1 μm were defined by electron beam lithography (EBL) and electron beam deposition of 3 nm Cr and 27 nm Au followed by lift off. A 1µl of ZnO coated peptide nanotube solution was dropped on the electrodes and allowed to dry at room temperature. Figure 3.1(d) inset shows an optical microscope image of a representative device, where a nanotube is connected to Au electrodes. Room temperature current-voltage (I-V) measurements were performed using a Keithley 2400 source-meter and a current pre-amplifier (DL 1211) capable of measuring sub pico-ampere signal interfaced with LABVIEW program. Figure 3.1(d) shows a schematic diagram of experimental measurements set up. A total of nine devices were investigated.

Figure 3.2 (a) I-V characteristics with full cycle sweep (-10 V→ +10 V→ -10 V) at ambient condition with a relative humidity of ~ 45%. (b) I-V characteristics for different sweep scan direction: (1) 0 to -10 V, (2) +10 to 0 V, (3) 0 to +10 V, and (4) +10 to 0 V scan rages. No NDR peaks were observed in the reverse-sweep direction 2 and 4. Sweep rate = 500 mV/sec (c) I-V characteristics of five consecutive sweeps with applied voltage ranges of 0 to +10 V. (d) I-V characteristics of different sweep rates from 250 to 750 mV/sec with 250 mV/sec intervals.

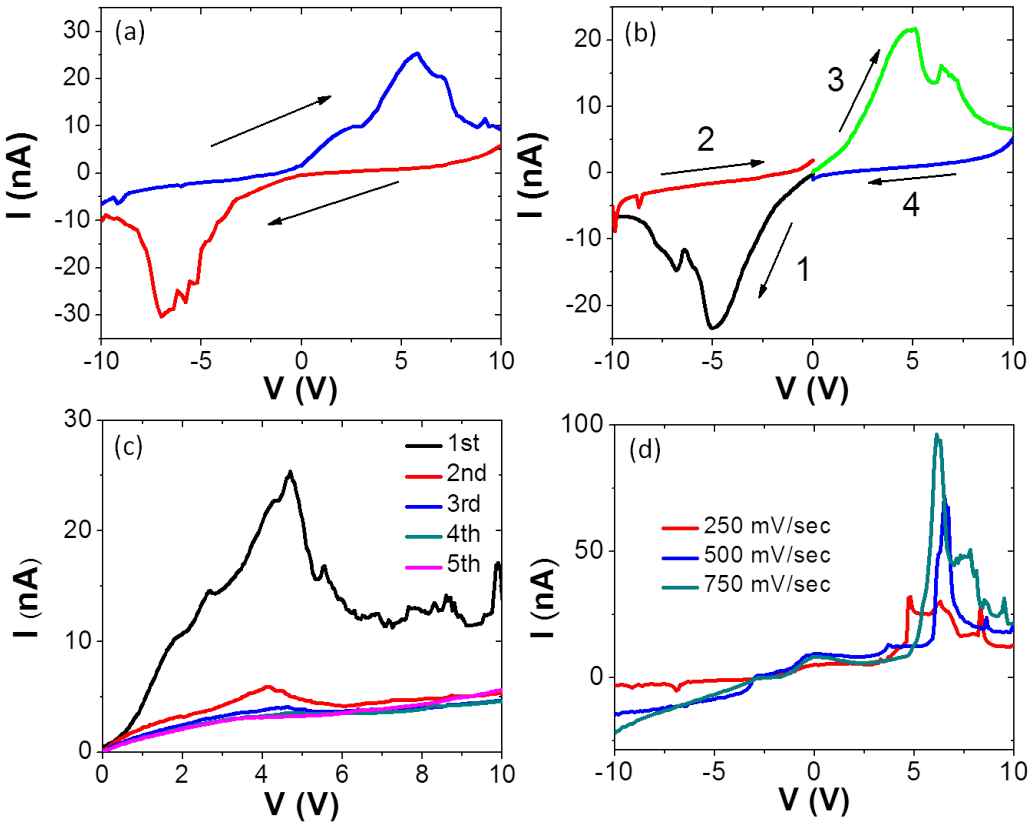

Results and Discussions

Figure 3.2 (a) shows the room temperature I-V characteristics of a representative device measured in ambient condition (humidity of ~ 45 %). The voltage was swept from - 10 to + 10 V (forward sweep) and then back to -10 V (reverse sweep) with a rate of ~ 500 mV/sec. A signature of NDR, decreasing current level with increasing voltage in I-V, was observed in both directions along with a hysteresis. In the forward sweep, the NDR peak was observed only at ~ 5.2 V with a peak to valley ratio (PVR) of ~ 3, while in the reverse sweep the peak position was observed at ~ - 7 V. It is important to note that NDR behavior occur with current rectification (rectification ratio is about ~ 10) similar to what has been observed in DNA based molecular devices. [55, 56, 58, 68] NDR behavior was also present when we started the sweep from zero bias. This scan is presented in Figure 3.2 (b) where we show I-V curve for different sweep scan directions: 0 to -10 V (1), -10 to 0 V (2), 0 to +10 V (3), and +10 to 0 V (4). Again, asymmetric NDR behavior is clearly observed. Most of our devices show similar NDR behaviors although there were slight variation in the NDR peak positions and current intensities from device to device. Additionally, the current in Figure 3.2 (a) did not vanish at zero bias in both negative and positive scans, indicative of contribution of capacitance due to trapping/detrapping of charges within the ZnO coated peptide nanotubes. [69]

In order to better understand the NDR mechanism, we measured continuous voltage scan on the devices without any relaxation time. Figure 3.2 (c) shows five consecutive I-V sweeps of the devices from 0 to +10 V. After the 4^{th} sweep, the NDR effects disappeared. The current ranges continuously decreased during subsequent sweep. Interestingly, the NDR reappeared again after the negative sweep. Also, NDR and current

ranges are recovered after a relaxation time of 5 minutes without any additional steps. The asymmetric NDR behavior along with rectification and the disappearance of NDR in successive sweep is different than recently reported NDR phenomenon in ZnO nanowires. [70] In these reports, NDR behavior has been explained due to resonant tunneling diode mechanism occurring as a result of tunnel junction at the contact between electrode and the ZnO. However, this mechanism cannot explain the hysteresis in NDR behavior.[71] Based on charge trapping and hysteric I-V curve, the NDR mechanism observed in our sample could be due to a reversible redox effect.[54]

Table 3.1 Sweep rate dependent on NDR and rectification properties. The values are taken from Figure 3.2 (d).

Scan rate (mV/sec)	MAX peak current (nA)	Rectification ratio
250	30.23	31.45
500	71.05	6.17
750	94.47	9.6

The redox effect can be further confirmed by measuring the I-V curves with different scan rate. This is shown in Figure 3.2 (d) where we study NDR peak position with different sweep rates from 250 to 750 mV/sec with 250 mV/sec intervals. During the measurement, we allowed 5 minutes of relaxation time between the scans. As seen in Figure 3.2 (d), the sweep rate has an effect on the peak current position, and current intensities. When the sweeping speed was increased, the peak current were also increased, however, the rectification ratio decreased. The highest rectification ratio of ~31 was observed for lowest sweep rate of 250 mV/sec. In Table 3.1, we summarized changes in NDR and rectification properties as a function of sweep scan rates. These results indicate that the rates of redox increase with increases of voltage sweep rates, increasing the NDR peak current. Similar behavior has been observed in DNA based molecule devices when the DNA devices interact with water molecules redox reaction.[58]

Figure 3.3 I-V characteristics under a relative humidity of 11 %. Blue line indicates the sweep voltage of from -10 to 10 V, while red line indicates the sweep voltages of from 10 to -10 V. No NDR and rectification have been observed.

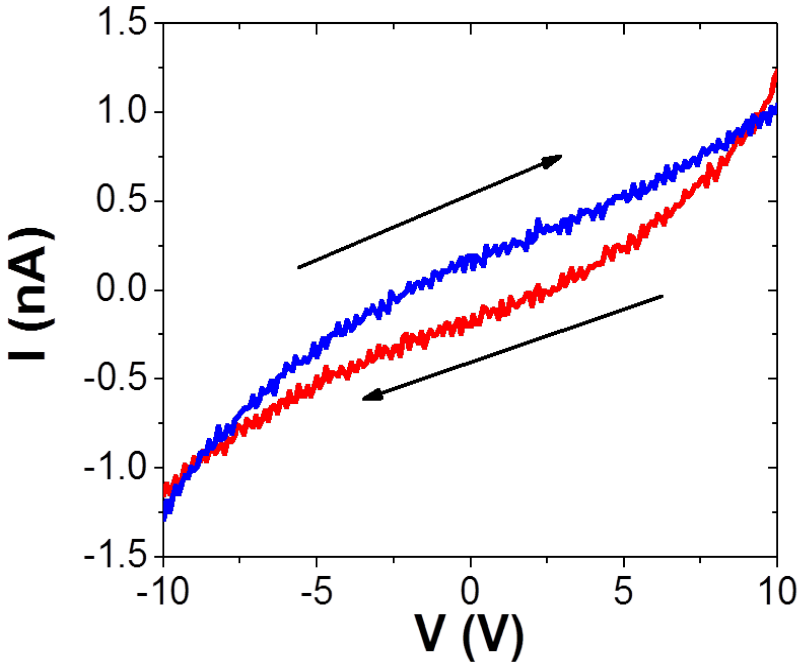

In order to further investigate the effects of redox water molecule reaction (or humidity) on the NDR device, we measured the I-V in a glove box with a humidity of 11 % as well as in a vacuum loaded cryostat (100 mTorr with ~ 0 % humidity). When the devices were measured at 11 % humidity, a significant decrease (over 20 times) in current was observed and the NDR effects were not observed, as shown in Figure 3.3. When the devices were measured under vacuum condition (humidity of 0 %) no measureable current (pA) was detected. Interestingly, after exposure to ambient condition with humidity of ~ 45 % for 10 minutes, the NDR behavior reappeared. Such change of humidity influence on current intensity and NDR change indicates the proton-exchange conduction (Grotthuss mechanism) [68, 72] through the water layer formed on the surface of ZnO: water is oxidized at the positively charged anode generating oxygen gas, the protons conduct through water layer on ZnO and reach the cathode where they are reduced to hydrogen gas by combing with electrons provided by the anode. If the drift of protons on ZnO is fast enough, the slow diffusion of water along ZnO [73] will deplete water around the anode causing the decrease in current and NDR.

In order to confirm the role of ZnO, we carried out a control experiment in ambient condition on the peptide nanotube without any ZnO coating. Neither the NDR, nor any detectable current were measured. Therefore, we conclude that the ZnO is a prerequisite to allow water molecules to absorb on its surface generating improved conductivity and NDR effects. In addition, the undetected measureable current under vacuum condition (~0% humidity) confirms that the electron hopping paths in amorphous ZnO film is very limited.[74] The conduction in low humidity (Figure 3.3) can be

explained by the hopping of electron through localized states in amorphous ZnO and through puddles of water across ZnO surface.

Conclusions

In summary, we demonstrate room temperature NDR in ZnO coated peptide nanotubes contacted with Au electrodes. The NDR have been shown in both positive and negative bias voltage ranges, and modulated by varying sweep scan rate and humidity. The highest rectification ratio of ~ 31 has also been observed. Interestingly, the properties are observed to disappear and recover by changes in sweep speed, relaxation time, and humidity. The NDR is due to the redox reaction of water molecules absorbed on the surface of ZnO coated peptide nanotubes. These results open up a simple way to construct bio-templated semiconductor device for biological sensor and logic circuit applications.

Chapter 4. One-Pod Crystalline ZnO Nanorod Growth in Peptide Mineralization Gels

Introduction

Znic Oxide, a semiconductor with a large direct band gap, possesses unique optical, acoustic, and electronic properties. ZnO is one of the most widely studied metal oxides for use in solar cell,[75] sensors,[76] ultraviolet nanolasers,[77] and blue-light-emitting diodes (LEDs).[78] This wide variety of applications requires the fabrication of ZnO nanostructures in distinct morphology and functionality. There is a growing interest in attempts to grow such inorganic nanoparticles in controlled morphology and structure by using biomolecular templates. One of the research motivations for this combination is to take advantage of the catalytic activity for the room-temperature material growth and the ability of self-assembly into controlled structures on a large scale.[8, 10-13]
Numerous peptides exhibiting high binding affinities for various inorganic materials were engineered using combinatorial library approaches such as phage display and cell-surface display,[14-19] and some of these peptides are capable to mediate the formation of specific inorganic material on templates incorporating these peptides. However, in many cases the coating of these mineralizing peptides on nanoscale templates and the morphology control on resulting peptide-coated templates are not straightforward for the subsequent metal growth.

In this paper, we developed a new approach for the one-pod synthesis of ZnO nanorod at neutral pH and room temperature; by self-assembling peptides which possess

the catalytic mineralization function for the specific oxide metal, ZnO nanorods (NRDs) can be grown as the peptides are assembled into rod structure. We optimized the growth conditions such as pH and precursor concentration to form monodisperse 1D NRDs and grow highly crystalline ZnO in both gelation and mineralization steps, and then one-pod synthesis of ZnO NRD was confirmed with the most optimized condition. A possible non-classical crystallization route is proposed for the ZnO-peptide NRD formation through amorphous $Zn(OH)_2$ gels confined by the peptide bundles. This new ZnO nano-structure synthesis may open a new strategy to design peptide as building blocks of inorganic nanomaterials.

Figure 4.1 (a) TEM image of peptide nanofibers in pH 7.0. (b) TEM image of peptide nanofibers in pH 10. (c) SAED of peptide nanofibers in pH 7.0 and pH 10. Scale bar = 100 nm.

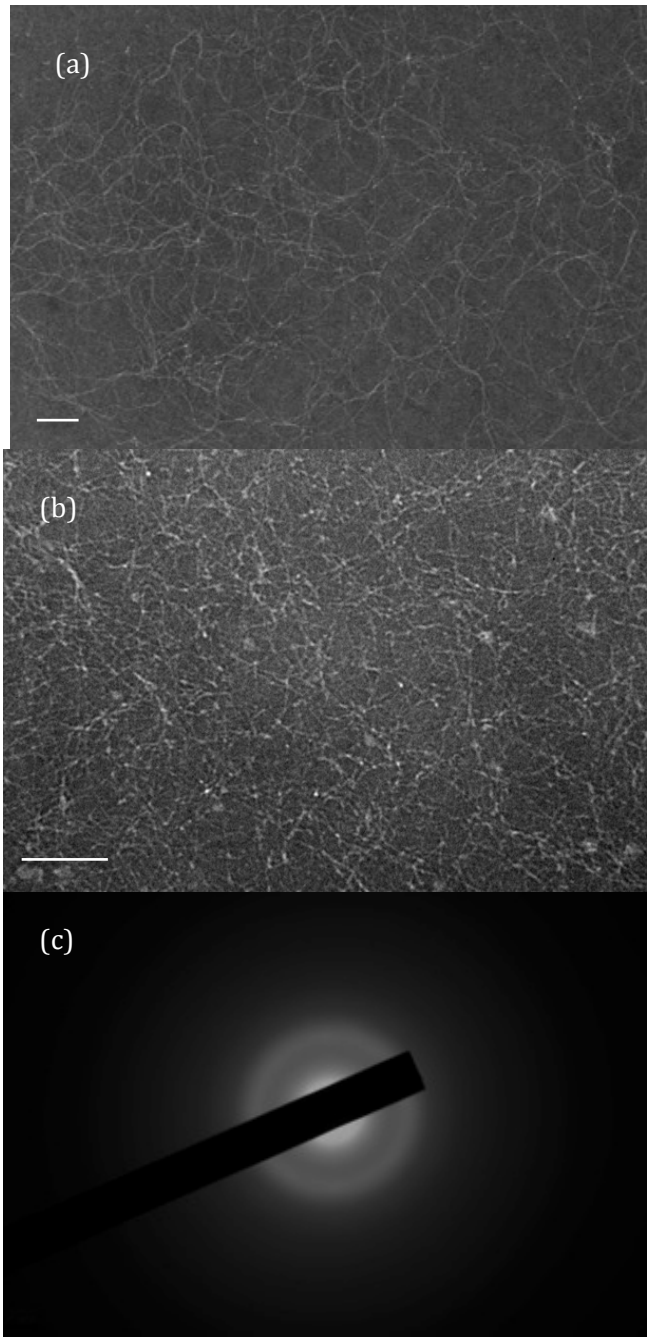

Results and Discussions

Previously, a ZnO-binding peptide ZnO-1 (EAHVMHKVAPRP) shows ZnO mineralization function after adding a five amino acids tail (GGGSC) to the C-terminal at room temperature.[15] Without the tail, ZnO-1 could not dehydrate $Zn(OH)_2$ to produce crystalline ZnO. There is another ZnO-binding peptide, CN111 (PAGLQVGFAVEV),[16] which is more hydrophobic and negatively charged around neutral pH.[79] Such properties of CN111 peptide should be more appropriate to enhance the affinity to zinc ions and the potential of self-assembly in aqueous solution. Therefore, CN111 with the dehydration tail of GGGSC (CN111-GGGSC peptide) has a potential to be assembled into fibers and then attract zinc ions for the crystalline ZnO growth through the dehydration process of intermediate $Zn(OH)_2$. To examine this hypothesis, first the CN111-GGGSC peptide was dissolved in 0.01 M pH 7.0 and pH10 phosphate buffer solution to observe its assembling property. After an overnight incubation, nanofibers in an average diameter of 3 nm and lengths ranging from hundreds of nanometers to several micrometers were observed in a transmission electron micrograph (TEM) (Figure 4.1). The electron diffraction pattern of the resulting nanofibers show a ring pattern (Figure 4.1c), corresponding to polycrystalline structure with an intermolecular distance around 3.8 Å. Almost no fibers were observed in a pH 3.0 solution where the peptide has no net charge at this pHs. From this observation, the balance between the hydrophobic interaction and electrostatic interaction seems to be important for the formation of peptide nanofibers.

Figure 4.2 (a) TEM images of the Zn^{2+} - peptide spherical gels observed in 0.1 mM peptide with 1.0 mM $Zn(Ac)_2$ at pH 7.0. Scale bar = 2 µm. (b) Close view of the gel in (a). Inset of (b) is the SAED of the gel at pH 7.0. Scale bar = 200 nm. (c) Magnified image of the gel structure in (b). Scale bar = 200 nm. (d) EDS on the Zn^{2+} - peptide spherical gels. (e) TEM images of the peptide nanofibers in 0.025 mM Zn, (f) 0.40 mM Zn, and (g) 1.0 mM Zn. (h) TEM image and SAED of the Ca^{2+} - peptide spherical gels observed in 0.1 mM peptide with $Ca(NO_3)_2$ in 0.025 mM at pH 7.0. Scale bar = 100 nm.

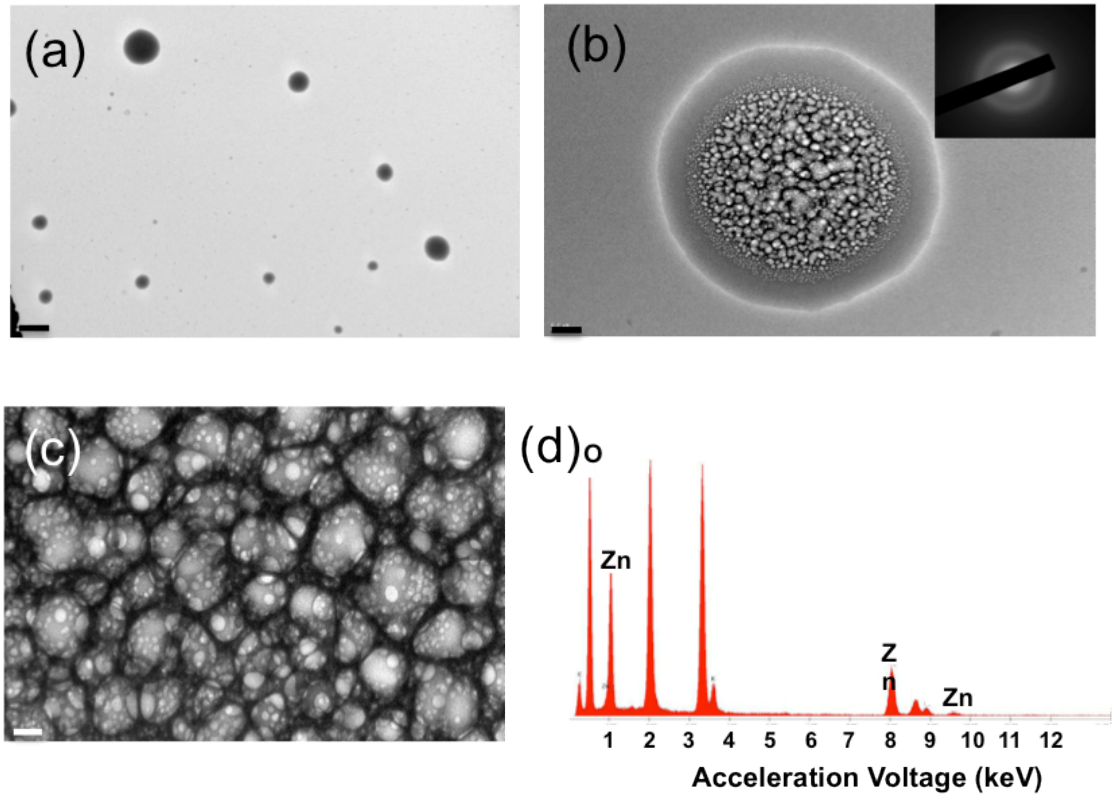

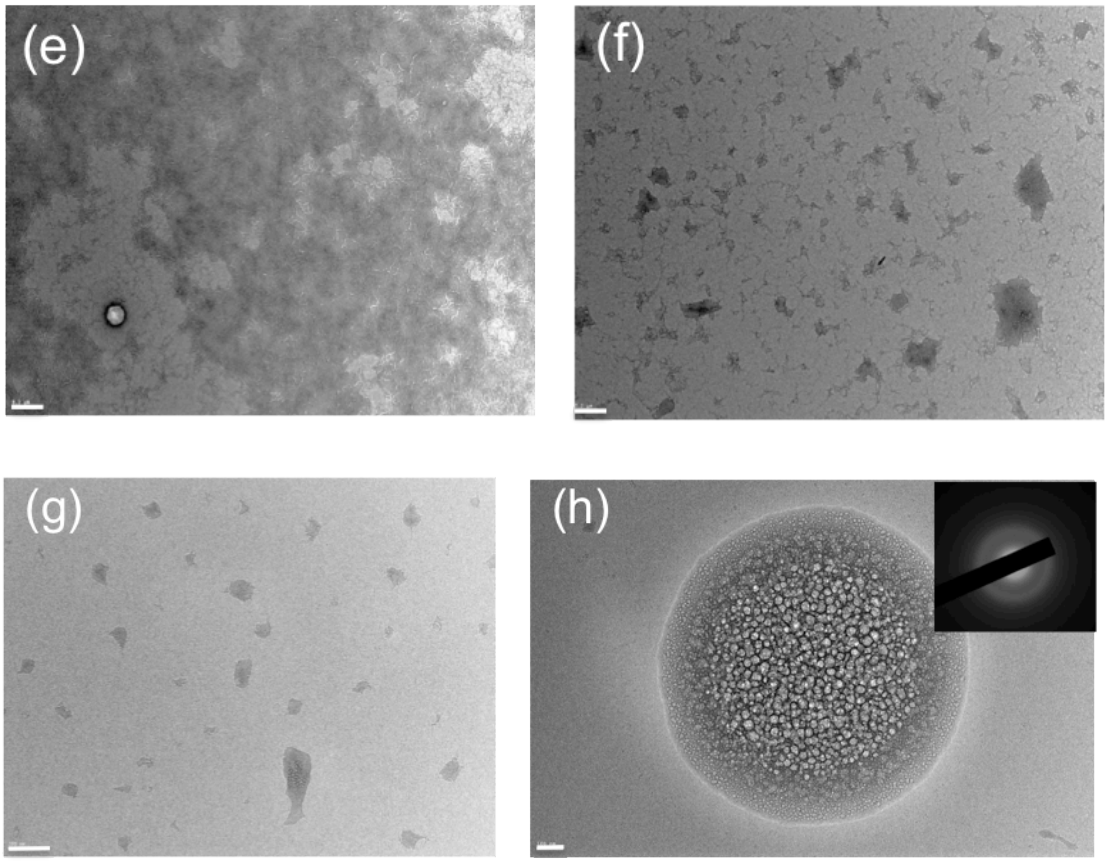

When zinc acetate ($Zn(Ac)_2$) was added and incubated in 0.1 mM peptide nanofiber-containing solution at pH 7.0, a new structure, the spherical gel in Figures 4.2 a-c, was observed. This gel includes zinc ions confirmed by the energy dispersive spectroscopy (EDS) as shown in Figure 4.2d. Since the diameter of the network branches in the gel agrees with the diameter of peptide nanofibers, SAED was applied to confirm whether these peptide nanofiber branches are really bundled the peptide nanofibers observed in Figure 4.1. The SAED pattern of this sample shows that the Zn^{2+} - peptide gel has polycrystalline nature of peptide with an intermolecular-distance around 3.8 Å, which exactly matches the diffraction pattern from the peptide-assembled nanofibers (inset of Figure 4.2b). The agreement of SAED patterns between Figures 4.2b and 4.1c suggests

that the gel consists of the bundles of peptide nanofibers. Besides, the number of the gels gradually increased when the concentration of $Zn(Ac)_2$ was increased from 0.025 mM to 1.0 mM (Figures 4.2e-g). Since the amount of peptide nanofibers in the background also decreased as the $Zn(Ac)_2$ concentration was increased in these images, this microscopic observation also indicates that the gels in Figure 4.2 contain peptide nanofibers and zinc ions, and we hypothesize that nanofibers are gelated with these amorphous Zn derivatives. Since pH has significant effect on the production of $Zn(OH)_2$, to examine this hypothesis we changed pH of the growth solution. At the concentration of 1 mM of $Zn(Ac)_2$, when pH was increased from pH 7.0, the smaller number of gels but more $Zn(OH)_2$ precipitates were observed at higher pHs where the condition is more favorable to produce $Zn(OH)_2$ (see Figure S4.1 in supplementary information). At lower pHs, the gel structure is still maintained by bundling peptide nanofibers with Zn ions and their derivatives. But at higher pHs, Zn ions in the gel start transforming to crystalline $Zn(OH)_2$, which in turn decreases the amount of gels due to the loss of the counter charges that holds the gel.

To better understand the role of charged ions in the formation of the peptide-bundled gels, calcium nitrate ($Ca(NO_3)_2$) was used to examine whether Ca^{2+} can replace Zn^{2+} for the formation of the peptide gels. As shown in Figure 4.2h, the gel was found in the solution of peptide and Ca^{2+}, and the same diffraction pattern of the peptide assembly observed in the Zn^{2+} peptide gel with the ~3.8 Å intermolecular distance was observed at pH 7 in the Ca^{2+} concentration of 0.025 ~ 0.1 mM. The existence of calcium in the gel was also confirmed in EDS, and the number of gels was also increased as Ca^{2+} concentration was increased. Thus, the electrostatic force between the negatively charged peptide fibers and

the positively charged divalent metal ions is the major driving force to generate the gel in Figure 4.2.

Figure 4.3 TEM images of (a) the ZnO-peptide NRDs in early growth stage (Scale bar = 200 nm) (b) the ZnO-peptide NRDs formed in 1.0 mM $Zn(Ac)_2$ (Scale bar = 200 nm), inset is the magnified image of the NRD surface (Scale bar = 20 nm). (c) EDS on the ZnO NRDs. (d) SAED on the ZnO-peptide NRDs. (e) HRTEM of the ZnO NPs on ZnO-peptide NRDs. Scale bar = 2 nm. (f) TEM image of the ZnO-peptide NRD formed in 0.025 mM $Zn(Ac)_2$ (scale bar = 500 nm). Inset is the magnified image on the NRD surface (scale bar = 5 nm).

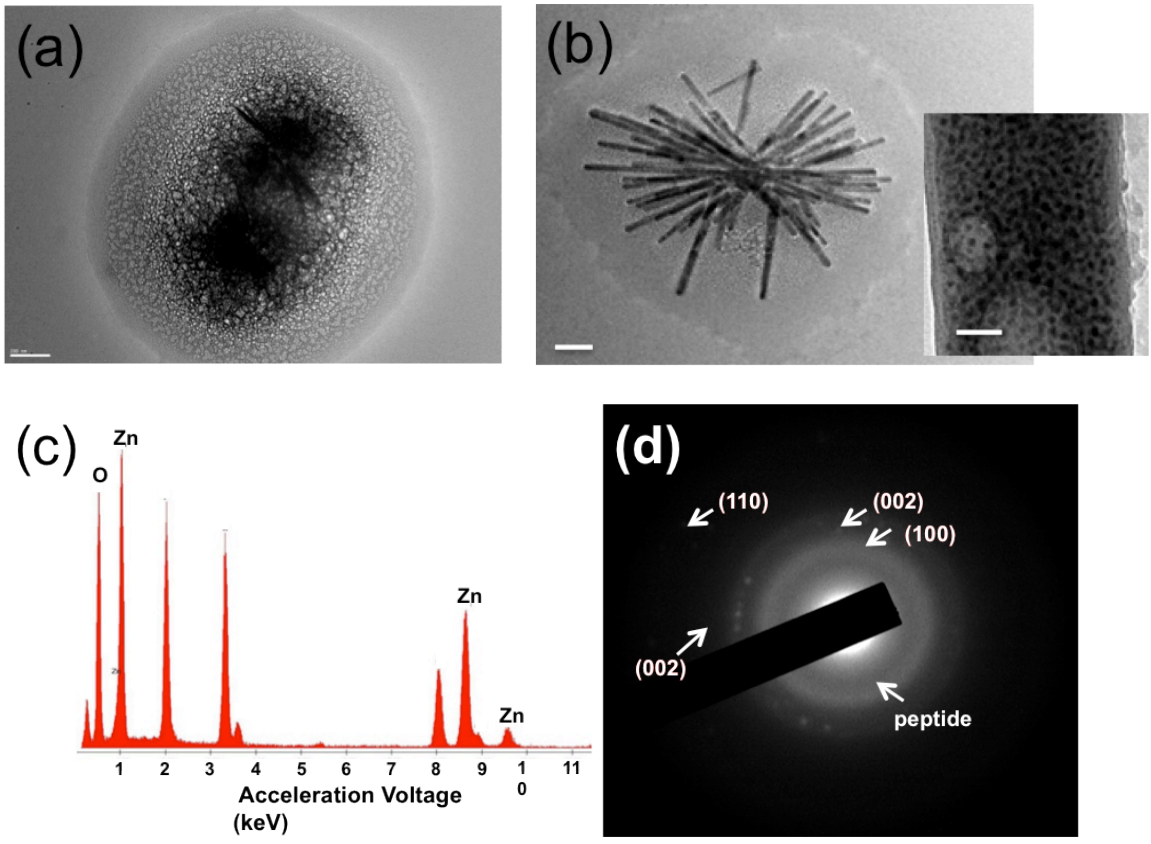

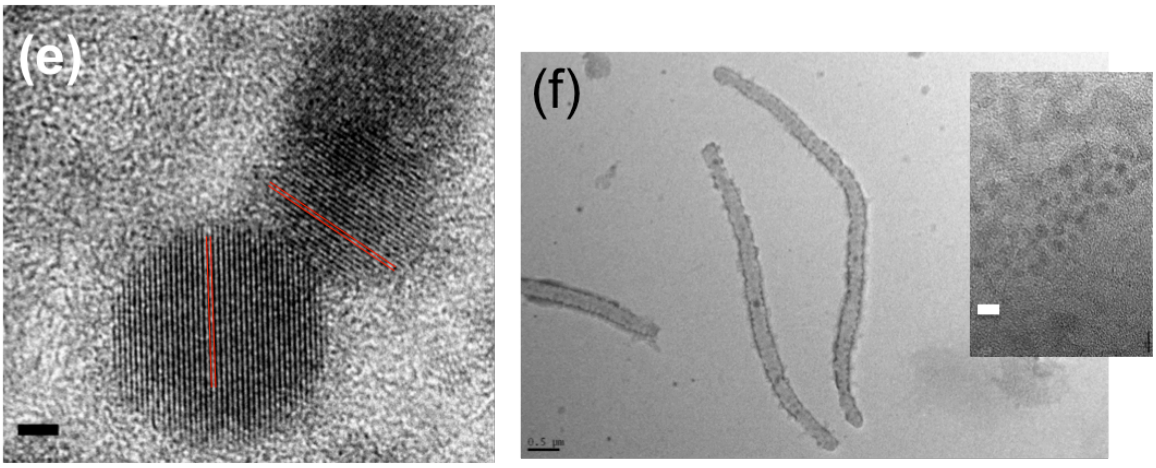

Our goal is to convert Zn ions on the peptide fibers in the peptide-bundled gel to ZnO for the formation of ZnO NRDs template on the mineralizing peptides. Based on the outcome from Figure 4.2, to accomplish this aim we need to add NaOH to introduce the formation of $Zn(OH)_2$ in the gel and induce slow hydrolysis of the Zn intermediates without triggering the complete decomposition of the gels. Therefore, for the ZnO growth we left the mixture in longer time in the mild growth condition to slowly hydrolyze without disassembling the gel. After the solution containing 0.1 mM peptide and 1 mM $Zn(Ac)_2$ was mixed with 3.5 mM NaOH to increase pH to 7.5 , the semi-rod structure of ZnO is appearing in the gel as shown in Figure 4.3a. After four days, ZnO nanoparticles (NPs) were coated on the peptide nanofibers with a size distribution of 30~80 nm in width, 600 nm to micrometer size in length and The ZnO NPs were in the diameters between 3 nm and 10 nm (Figure 4.3b). Since the dimension of NRDs is similar to the peptide nanofibers except the width, it is likely that the side-by-side bundled peptides template the ZnO NRD growth. The EDS shows the high zinc signal on the dark rod surface (Figure 4.3c), and the SAED shows (100), (002), and (110) planes of ZnO (Figure 4.3d). In the high-resolution transmission electron micrograph (HRTEM), ZnO (002)

lattice fringe can be clearly observed (Figure 4.3e). In addition, the SAED also shows the assembly of peptide nanofibers with the intermolecular distance of ~3.8 Å, indicating that the peptide nanofibers are templated for the formation of crystalline ZnO NRDs (Figure 4.3d). In a control experiment with much less [$Zn(Ac)_2$], 0.025 mM, very few ZnO NPs were covered on the rod surface, and the rods look less rigid (Figure 4.3f). This indicates that increased [Zn^{2+}] will lead to increase the density of ZnO NP coating and this increased coating coverage reinforces the resulting nanorod structure. In another control experiment grown in the same condition without the peptide, only $Zn(OH)_2$ microcrystals are observed (see Figure S4.2 in supplementary information).

Figure 4.4 (a) TEM image of the gels right after synthesis, and (b) after two months. Scale bar = 400 nm. (c) High resolution TEM image of the surface of ZnO NRD right after the synthesis, and (d) after two months. Scale bar = 20 nm. (e) SAED of the gels surrounding ZnO NRDs. (f) ZnO NRDs formed by the one-pot synthesis at pH 7.5 (scale bar = 200 nm). Inset is the ZnO NRD in higher magnification (scale bar = 60 nm).

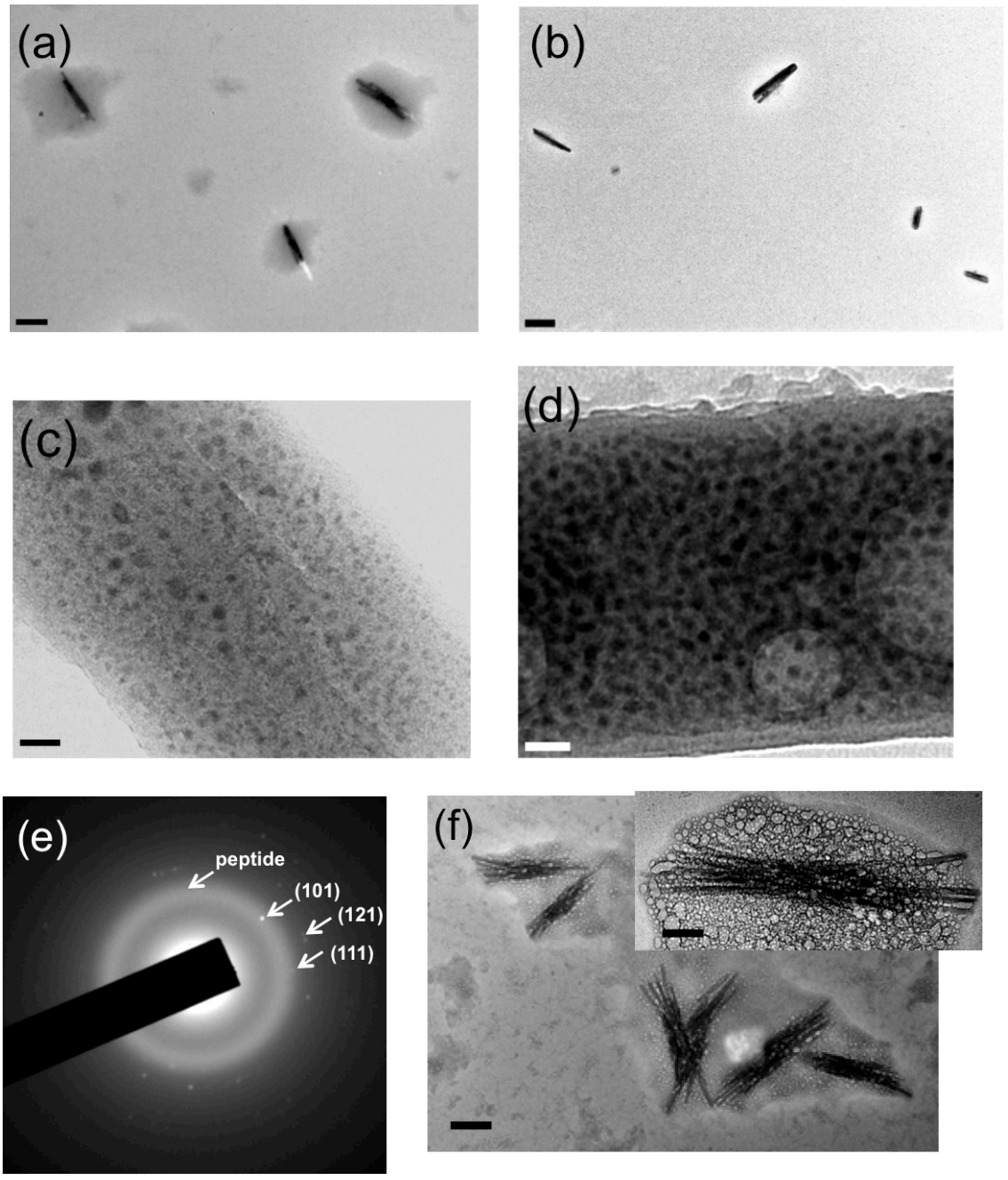

If our hypothesis about the conversion of amorphous $Zn(OH)_2$ intermediates in the gel to ZnO is correct, $Zn(OH)_2$ near the peptide nanofibers should be converted to crystalline ZnO and thus the volume of the gel should be reduced via this conversion with time. As compared with the gel reacted for four days (Figure 4.4a), the gel incubated for two months reduced the size of gel around ZnO NRDs (Figure 4.4b) in the same condition. In addition, the surface area of ZnO NPs coated on the NRDs (Figure 4.4c) increases as the gel shrinks with time (Figure 4.4d) and after two months SAED of the gel surrounding ZnO NRDs show the diffraction pattern consisting of both peptide nanofibers and $Zn(OH)_2$ (Figure 4.4e). All of these results indicate that $Zn(OH)_2$ formed at pH 7.5 in the gel around peptide nanofibers is the precursor of the crystalline ZnO growth and the conversion occurs in the gel. All of these results indicate that the gel containing $Zn(OH)_2$ and peptide is the source or reaction matrix of ZnO NRDs. It should be noted that crystalline $Zn(OH)_2$ in the solution outgrows the peptide nanofiber-assembled gel at higher pH because of the reduction of available Zn ions for the gel formation (see Figure S4.1 in supplementary information).

On the basis of a series of experiments we examined, ZnO NRDs are only observable through the formation of the $Zn(OH)_2$–peptide gels as intermediates. Without the peptides, only crystalline $Zn(OH)_2$ is formed, and when pH of the growth solution is too high overgrown $Zn(OH)_2$ in solution consumes a majority of zinc ions necessary for the assembly of peptide nanofibers in the gel form and therefore there observe less ZnO NRDs. The proper balance between certain pH and concentration ranges enables the growth of peptide nanofibers coated by densely packed ZnO nanocrystals via formation of the peptide-zinc ion gels.

When the peptide was incubated with $Zn(Ac)_2$ at pH 7.5 for 5 days, this one-pod condition also enables growing ZnO NRDs in the same order of high crystallinity (Figure 4.4f). The dimension of NRDs and the formation of gel media around NRDs are quite similar to the ones in Figure 4.3. This demonstration indicates that the optimized condition can be applied to grow highly crystalline ZnO NRDs in one step.

Conclusions

The ZnO-binding peptide CN111-GGGSC (PAGLQVGFAVEVGGGSC) is shown to assemble into nanofibers and its mineralization function enables growing crystalline ZnO NPs on these peptide nanofibers. These peptides are self-assembled into 3 nm wide, and the lengths are ranging from hundreds of nanometers to several micrometers in neutral to basic (pH 10) water solution. Addition of divalent metal ions such as Zn^{2+} and Ca^{2+} induces gelation of peptide nanofibers due to the electrostatic interaction between positively charged metal ions and negatively charged peptides. After four days of incubation around neutral pHs, amorphous $Zn(OH)_2$ inside the gel is dehydrated by the CN111-GGGSC peptide to produce ZnO NP coating on the peptide nanofibers. The consumption of amorphous zinc derivatives in the gel is observed as the gel volume is reduced and ZnO coating area is increased in TEM images with time. The highly crystalline ZnO NRDs can also be grown in one-pod in the condition optimized in gelation and mineralization steps. A possible route for the ZnO-peptide NRD formation from the peptide nanofibers is proposed where amorphous intermediate is an energetically efficient path to grow crystalline nanoparticles with high yield.

In this work, we combine the self-assembly and the mineralization properties of peptides to synthesize ZnO NRDs without using preformed templates under mild and environmentally benign conditions – neutral pH and room temperature. This outcome will help identify novel peptides which possess both the self-assembly and biomineralization functions to generate desired materials by the peptide design.

Experimental Section

Preparation of Peptide Nanofibers: CN111-GGGSC peptide, PAGLQVGFAVEVGGGSC, was purchased from GenScript with an 85 % purity. 0.01 M phosphate buffer at pH 3.0, pH 7.0 and pH 10 were used separately to dissolve peptide powder and make 0.1 mM peptide solutions and incubate overnight at room temperature. Peptides were self-assembled into nanofibers in pH 7.0 and pH 10 buffer solutions. Almost no nanofibers were found in pH 3.0 buffer solution.

Synthesis of ZnO NRDs: Typically, to generate ZnO NRDs, first 100 μl of CN111-GGGSC peptide (0.1 mM) in pH 7.0 phosphate buffer solution were prepared. Zinc acetate ($Zn(Ac)_2$, Sigma-Aldrich) at different concentrations (0.025 mM ~ 1.0 mM) were added and incubated with peptide nanofiber solution overnight. Drops of 1 M NaOH was added and incubated with nanofiber solution containing Zinc ions for four days to grow $Zn(OH)_2$,and the extra amount of NaOH beside forming $Zn(OH)_2$ were adding there to adjust different incubation pH from 7.0 to pH 7.5 and higher pH. In the control experiment to examine the influence of divalent metal ions on the gelation of peptides,

calcium nitrate ($Ca(NO_3)_2$, Sigma-Aldrich) was used instead of $Zn(Ac)_2$,with exactly same experiment conditions as using $Zn(Ac)_2$.

One-Pod synthesis of ZnO NRDs from peptides: CN111-GGGSC peptide powder, 0.0011 g, was added in 7.0 ml pH 7.0 PBS (0.01M) buffer solution, which makes the peptide concentration as 0.1 mM, immediately followed by adding 0.0013 g $Zn(Ac)_2$ to make the concentration as 1.0 mM of zinc precursor. This step enables formation of the peptide gels bundled by zinc ions. Then, 3.5 mM of NaOH was added for forming $Zn(OH)_2$, and adjusting pH from 7.0 to pH 7.5 to convert all of the zinc precursor to $Zn(OH)_2$. The solution was well mixed and incubated for 5 days. Then these $Zn(OH)_2$ will be converted into ZnO due to the dehydration function of the CN111-GGGSC peptide. This condition was optimized by previous two-step evaluation to grow ZnO-peptide NRDs but the volume of the peptide solution was increased from 100μl to 7.0 ml due to the convenience of experimental procedure.

Characterization: The morphology of peptide nanofibers and ZnO coated structures were characterized by high-resolution transmission electron microscopy (HRTEM – JEOL JEM-2100). Peptide nanofiber specimens were negative stained by 1 % Ammonium Molybdate before using HRTEM. Peptide nanofiber with zinc/calcium ions specimens were tested without staining. Selected area electron diffraction (SAED) were used to study the structural natures of peptide nanofiber, ZnO, and $Zn(OH)_2$ in the gels. Energy-dispersive spectroscopy (EDS, EDAX Inc.) was used to examine the existence of zinc or calcium elements in selected areas in the gels.

Supplementary Information

When ZnO nanorod (NRD) was formed at pH 7.5 with 0.1 mM CN111-GGGSC (PAGLQVGFAVEVGGGSC) peptide and 1.0 mM $Zn(Ac)_2$, the coating domain of ZnO NPs is most monodisperse and closed-packed with highest crystallinity. When the ZnO NRDs are grown at pH 8.0 instead of pH 7.5 by adding extra amount of NaOH solution, the amount of ZnO NRDs and the size of gels are decreased. At the same time, as pH is increased, more sheet-like microcrystalline $Zn(OH)_2$ starts appearing as shown in Figure S4.1a. SAED at the edge of these $Zn(OH)_2$ sheets shows characteristic diffraction pattern of the peptide nanofiber, ~3.8 Å, in addition to $Zn(OH)_2$ diffraction pattern (Figure S4.1b). When Zn NRDs are grown at pH9.0, very few of ZnO NRDs are observed. The amount and the size of $Zn(OH)_2$ microcrystalline sheet increase even more at this pH (Figures S4.1c-d). Again, at the edge of these crystal, the peptide diffraction pattern appears in the SAED along with the $Zn(OH)_2$ diffraction pattern (Figure S4.1e). And SAED near the center of crystal sheet shows a single crystalline pattern of $Zn(OH)_2$ (Figure S4.1f). In pH 8.0 and pH9.0, pH of the growth solution is too high so that overgrown $Zn(OH)_2$ in solution consumes a majority of zinc ions necessary as counter ions to assemble peptide nanofiber bunldes in the gel and therefore there observe less ZnO NRDs in the higher pHs.

In a control experiment to mix all growth solutions except the peptide, no ZnO NRDs and gel structures were observed and only the $Zn(OH)_2$ microcrystalline sheets appeared (Figure S4.2). The yield of microcrystalline $Zn(OH)_2$ follow the same trend that observed in experiment with peptide in different pH solutions: microcrystalline $Zn(OH)_2$ gradually increases when pH are increased from pH7.5 to pH9.0.

Figure S4.1 (a) TEM images of sheet-like microcrystalline structure of $Zn(OH)_2$ grown in pH 8.0 solution. Scale bar = 1 μm. (b) SAED of (a). (c) Microcrystalline structure of $Zn(OH)_2$ grown in pH 9.0 solution. Scale bar = 20 μm. (d) The closer-view of (c). Scale bar = 500 nm. (e) SAED at edge of (c). (f) SAED near center of (c).

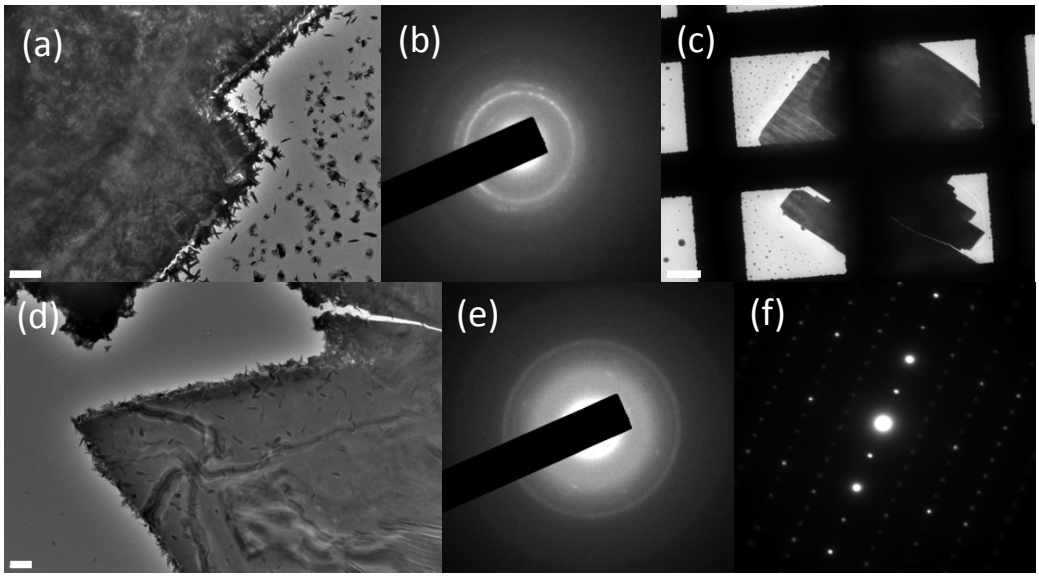

Figure S4.2 Microcrystalline structure of $Zn(OH)_2$ grown in the same experimental condition in 1.0 mM $Zn(Ac)_2$ and pH 7.5 as Figure 4.3 without the peptide. Inset is the SEAD of microcrystalline $Zn(OH)_2$. Scale bar = 20 μm.

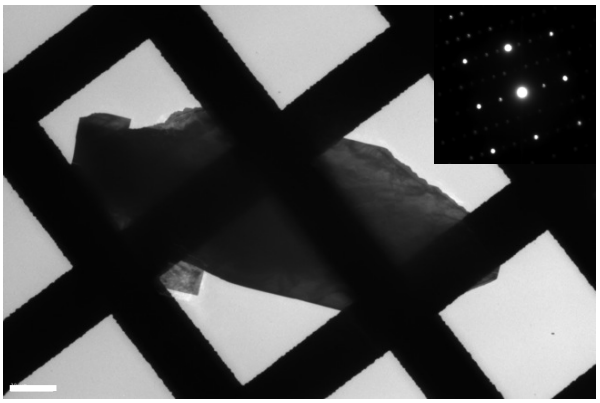

References

[1] M. E. Stewart, C. R. Anderton, L. B. Thompson, J. Maria, S. K. Gray, J. A. Rogers, R. G. Nuzzo, *Chem. Rev*. 2008, **108**, 494.

[2] E. V. Shevchenko, D. V. Talapin, N. A. Kotov, S. O'Brien, C. B. Murray, *Nature* 2006, **439**, 55.

[3] C. B. Murray, C. R. Kagan, M. G. Bawendi, *Annu. Rev. Mater.* 2000, **30**, 545.

[4] B. A. Kogel, S. Fullam, S. Connolly, D. Fitzmaurice, *J. Phys. Chem. B* 1998, **102**, 8379.

[5] D. V. Talapin, E. V. Schevchenko, A. kornowski, N. Gaponik, M. Haase, A. L. Rogach, H. Weller, *Adv. Mater.* 2001, **13**, 1868.

[6] E. Dujardin, C. Peet, G. Stubbs, J. N. Culver, S. Mann, *Nano Lett.* 2003, **3**, 413.

[7] S. Behrens, K. Rahn, W. Habicht, K. –J. Bohm, H. Rosner, E. Dinjus, E. Unger, *Adv. Mater.* 2002, **14**, 1621.

[8] R. Djalali, Y. –F. Chen, H. Matsui, *J. Am. Chem. Soc.* 2003, **125**, 5873.

[9] I. A. Banerjee, L. Yu, H. Matsui, *J. Am. Chem. Soc.* 2005, **127**, 16002.

[10] C. M. Niemeyer, *Angew. Chem. Int. Ed.* 2001, **40**, 4128.

[11] E. D. Sone, S. I. Stupp, *J. Am. Chem. Soc*. 2004, **126**, 12756.

[12] C. L. Chen, P. J. Zhang, N. L. Rosi, *J. Am. Chem. Soc*. 2008, **130**, 13555.

[13] S. Shekhar, L. Anjia, H. Matsui, S. I. Khondaker, *Nanotechnology* 2011, **22**, 095202.

[14] M. Sarikaya, C. Tamerler, A. K. Y. Jen, K. Schulten, F. Baneyx, *Nat. Mater.* 2003, **2**, 577.

[15] M. Umetsu, M. Mizuta, K. Tsumoto, S. Ohara, S. Takami, H. Watanabe, I. Kumagai, T. Adschiri, *Adv. Mater*. 2005, **17**, 2571.

[16] C. K. Thai, H. X. Dai, M. S. R. Sastry, M. Sarikaya, D. T. Schwartz, F. Baneyx, *Biotechnol. Bioeng.* 2004, **87**, 129.

[17] S. Brown, M. Sarikaya, E. Johnson, *J. Mol. Biol*. 2000, 299, 725.

[18] Y. Huang, C. Y. Chiang, S. K. Lee, Y. Gao, E. L. Hu, J. De Yoreo, A. M. Belcher, *Nano Lett*. 2005, **5**, 1429.

[19] K. T. Nam, D. W. Kim, P. J. Yoo, C. Y. Chiang, N. Meethong, P. T. Hammond, Y. M. Chiang, A. M. Belcher, *Science* 2006, **312**, 885.

[20] X. Gao, H. Matsui, *Adv. Mater.* 2005, **17**, 2037.

[21] L.Yu, I. A. Banerjee, H. Matsui, *J. Mater. Chem.* 2004, **14**, 739.

[22] L. Yu, I. A. Banerjee, M. Shima, K. Rajan, H. Matsui, *Adv. Mater.* 2004, **16**, 709.

[23] I. A. Banerjee, L. Yu, H. Matsui, *Proc. Natl. Acad. Sci. USA* 2003, **100**, 14678.

[24] L. Yu, I. A. Banerjee, H. Matsui, *J. Am. Chem. Soc.* 2003, **125**, 14837.

[25] G. J. Douberly, S. Pan, D. Walters, H. Matsui, *J. Phys. Chem. B* 2001, **105**, 7612.

[26] I. A. Banerjee, G. Muniz, S. –Y. Lee, H. Matsui, *J. Nanosci. Nanotechno.* 2007, **7**, 1.

[27] M. Shi, W. Su, H. Matsui, Nanosc. 2010, 2, 2373.

[28] NHBP-1 was originally isolated as a aptamer against carbon naohorns (Kase et al. *Langmuir* 2004, **20**, 8939). Subsequent studies have revealed that the peptide possesses the abilities of "self-assembling" (Sano et al, *Prot. Eng. Des. Select.* 2007, **20**, 109;

Matsui et al, *Langmuir* 2007, **23**, 1615) and "Au mineralization" (KS, unpublished), in addition to the carbon material-binding activity.

[29] Obtained using the peptide property calculator at Innovagen (http://www.innovagen.se)

[30] C. -b. Mao, C. E. Flynn, A. Hayhurst, R. Sweeney, J. –f. Qi, G. Georgiou, B. Iverson, A. M. Belcher, *Proc. Natl. Acad. Sci. USA* 2003, **100**, 6946.

[31] D. V. Talapin, J. S. Lee, M. V. Kovalenko, E. V. Shevchenko, *Chem. Rev.* 2010, **110,** 389.

[32] M. C. Daniel, D. Astruc, *Chem. Rev.* 2004, **104**, 293.

[33] A. M. Smith, A. M. Mohs, S. Nie, *Nat. Nanotechnol.* 2009, **4,** 56.

[34] B. Weidenhof, M. Reiser, K. Stowe, W. F. Maier, M. Kim, J. Azurdia, E. Gulari, E. Seker, A. Barks, R. M. Laine, *J. Am. Chem. Soc.* 2009, **131,** 9207.

[35] A. Zabet-Khosousi, A. A. Dhirani, *Chem. Rev.* 2008, **108,** 4072.

[36] Z. Nie, A. Petukhova, E. Kumacheva, *Nat. Nanotechnol.* 2010, **5,** 15.

[37] Y. Huang, X. Duan, Q. Wei, C. M. Lieber, *Science* 2001, **291,** 630.

[38] A. M. Hung, C. M. Micheel, L. D. Bozano, L. W. Osterbur, G. M. Wallraff, J. N. Cha, *Nat. Nanotechnol.* 2010, **5,** 121.

[39] Y. J. Lee, H. Yi, W. –J. Kim, K. Kang, D. S. Yun, M. S. Strano, G. Ceder, A. M. Belcher, *Science* 2009, **324,** 1051.

[40] I. Yamashita, *J.Mater.Chem.* 2008, **18**, 3813.

[41] T. Matsui, N. Matsukawa, K. Iwahori, K. –I. Sano, K. Shiba, I. Yamashita, *Langmuir* 2007, **23,** 1615.

[42] A. A. Middleton, N. S. Wingreen, *Phys.Rev.Lett.* 1993, **8**, 3198.

[43] M. G. Ancona, W. Kruppa, R. W. Rendell, A. W. Snow, D. Park, J. B. Boos, *Phys. Rev.* B 2001, **64,** 033408.

[44] P. Beecher, E. V. Shevchenko, H. Weller, A. J. Quinn, G. Redmond, *Adv. Mater.* 2005, **17,** 1080.

[45] R. Parthasarathy, X. M. Lin, H. M. Jaeger, *Phys. Rev. Lett.* 2001, **87,** 186807.

[46] G. Iversen, Y. I. Kharkats, J. Ulstrup, *J. Inorg. Biochem.* 1995, **59,** 350.

[47] C. T. Black, C. B. Murray, R. L. Sandstrom, S. Sun, *Science* 2000, **290,** 1131.

[48] K. C. Beverly, J. L. Sample, J. F. Sampaio, J. R. Heath, R. D. Levine, *Proc. Natl Acad. Sci. USA* 2002, **99,** 6456.

[49] C. A. Neugebauer, M. B. Webb, *J. Appl. Phys.* 1962, **33,** 74.

[50] I. S. Beloborodov, A. V. Lopatin, V. M. Vinokur, *Rev. Mod. Phys.* 2007, **79,** 469.

[51] S. I. Khondaker, I. S. Shlimak, J. T. Nicholls, M. Pepper, D. A. Ritchie, *Phys. Rev.* B 1999, **59,** 4580.

[52] L.Esaki, *Phys. Rev.* 1958, **109,** 603.

[53] T. Sollner, W. Goodhue, P. Tannenwald, C. Parker, and D. Peck, *Appl. Phys. Lett.* 1983, **43,** 588.

[54] J. Chen, M. A. Reed, A. M. Rawlett, and J. M. Tour, *Science* 1999, **286,** 1550.

[55] J. He and S. M. Lindsay, *J. Am. Chem. Soc.* 2005, **127,** 11932.

[56] Q. Tang, H. K. Moon, Y. Lee, S. M. Yoon, H. J. Song, H. Lim, and H. C. Choi, J. *Am. Chem. Soc.* 2007, **129,** 11018.

[57] Y. Yang, J. Qi, Q. Liao, W. Guo, Y. Wang, and Y. Zhang, *Appl. Phys. Lett.* 2009, **95,** 123112.

[58] P. Jangjian, T. Liu, M. Li, M. Tsai, and C. Chang, *Appl. Phys. Lett.* 2009, **94,** 043105.

[59] R. de la Rica, C. Pejoux, and H. Matsui, *Adv. Funct. Mater.* 2011, **21,** 1018.

[60] S. Zhang, *Nat. Biotechnol.* 2003, **21,** 1171.

[61] C.-L. Chen and N. L. Rosi, *Angew. Chem. Int. Ed.* 2010, **49,** 1924.

[62] Y. S. Nam, A. P. Magyar, D. Lee, J.-W. Kim, D. S. Yun, H. Park, T. S. Pollom, D. A. Weitz, and A. M. Belcher, *Nat. Nanotechnol.* 2010, **5,** 340.

[63] X. Dang, H. Yi, M.-H. Ham, J. Qi, D. S. Yun, R. Ladewski, M. S. Strano, P. T. Hammond, and A. M. Belcher, *Nat. Nanotechnol.* 2011, **6,** 377.

[64] K. T. Nam, D.-W. Kim, P. J. Yoo, C.-Y. Chiang, N. Meethong, P. T. Hammond, Y.-M. Chiang, and A. M. Belcher, *Science* 2006, **312,** 885.

[65] R. J. Tseng, C. Tsai, L. Ma, J. Ouyang, C. S. Ozkan, and Y. Yang, *Nat. Nanotechnol.* 2006, **1,** 72.

[66] H. Matsui and B. Gologan, *J. Phys. Chem. B* 2000, **104,** 3383.

[67] A. van Dijken, E. A. Meulenkamp, D. Vanmaekelbergh, and A. Meijerink, *J. Phys. Chem. B* 2000, **104,** 1715.

[68] H. Lee and M. H. Jin, *Appl. Phys. Lett.* 2010, **97,** 013306.

[69] Y. Lin, P. Wu, C. Tsai, C. Liu, Z. Lin, H. Chang, and C. Lee, *J. Appl. Phys.* 2008, **103,** 113709.

[70] W. Guo, Y. Yang, J. Qi, and Y. Zhang, *Appl. Phys. Lett.* 2010, **97,** 263118.

[71] N. P. Guisinger, N. L. Yoder, and M. C. Hersam, *Proc. Natl. Acad. Sci. U.S.A.* 2005, **102,** 8838.

[72] M. E. Tuckerman, D. Marx, and M. Parrinello, *Nature* 2002, **417,** 925.

[73] M. Nagao, *J. Phys. Chem.* 1971, **75,** 3822.

[74] D. Cho, J. H. Kim, and C. S. Hwang, *Appl. Phys. Lett.* 2011, **98,** 222108.

[75] B. O'Regan, D. T. Schwarthz, S. M. Zakeeruddin, M. Grätzel, *Adv. Mater.* 2000, **12**, 1263.

[76] H. M. Lin, S. J. Tzeng, P. J. Hsiau, W. L. Tsai, *Nanostruct. Mater.* 1998, **10**, 465.

[77] M. H. Huang, S. Mao, H. Feick, H. Yan, Y. Wu, H. Kind, E. Weber, R. Russo, P. Yang, *Science* 2001, **292**, 1897.

[78] A. Tsukazaki, A. Ohtomo, T. Onuma, M. Ohtani, T. Makino, M. Sumiya, K. Ohtani, S. F. Chichibu, S. Fuke, Y. Segawa, H. Ohno, H. Koinuma, M. Kawasaki, *Nat. Mater.* 2005, **4**, 42.

[79] Obtained using the peptide property calculator at Innovagen (http://www.innovagen.se).